UNIVERSIDADE DE LISBOA
FACULDADE DE CIÊNCIAS
DEPARTAMENTO DE FÍSICA

Radiometry of an Integrating Sphere for Telescopes with a Fibre-Fed Spectrograph

Andreia Guerreiro Domingos

Mestrado Integrado em Engenharia Física

Dissertação orientada por:
Prof. Dr. Alexandre Pereira Cabral

2022

Dedicated to every dreamer: it's okay to fall down to earth.

Acknowledgments

First of all, I would like to express my deepest gratitude to Dr. Alexandre Cabral for accepting me as his student, for his (enormous) patience, for his knowledge, for his guidance and support, and mostly for not giving up on me when he could or should have.

Second, I would like to thank the Laboratório de Óptica, Lasers e Sistemas (LOLS) team from the physics department of the faculty of science of the University of Lisbon for their support provided and especially Tec. Fernando Monteiro for all the help with the equipment. (I will bring cake and cheese next time.)

People say that the best years of our life are college; it may be true for some, but for me it was not quite true. My life and struggles in college would not be surpassed if it weren't for the help of course colleagues and friends. A big fat thank you to Madalena Valente and Daniel Vilhena, they were there since day one, for every moment, the good, 'eh' and bad moments (specially those), and they are still here. Thank you Inês Figueira and Sofia Fonseca, although we met in the middle, our friendship stayed for good. Thank you Inês Leite, if it weren't for you, I would not have survived the pandemic and another depression when I started this thesis. Thank you Nuno Gonçalves for everything since day one as well, even though we are totally different we never stopped supporting each other. Thank you Manuel Xarepe and Pedro Rato for all the explanations and late night games with hot choco. I'm proud of you all!

But college is not everything in life. Thank you Mariana Leite, João Marcão, Carolina Catarino, Guilherme Roque, Ricardo Honório, Andreia Meseiro and Andreia Ribeiro, for giving me breaks in life, adventures to remember, hobbies to go back to, all your motivation and support. Your little things made my days.

Last but no least, I would like to express my deepest gratitude to Rui Vieira. You caught me and never let me fall again. You believed in me when I did not. You gave me strength when I hadn't any. Thank you love.

And if it weren't for you, for your support and all your nagging, I would not have this opportunity. Thank you mom, dad, big sis, grandma and grandpa.

You all helped me grow in your own way, personally and professionally, and I think that is the best experiment in life.

For real.

Million thanks.

Abstract

Astronomical instrumentation is one of the areas were optics have seen recently a considerable evolution, and spectroscopic observations of astronomical objects is one of the key subjects.

The goal of this thesis is to study integrating spheres, within the scope of astronomical instrumentation, an optical component that will enable the integration of sunlight for further injection into a spectrograph, by means of an optical fibre.

For this study, it is fundamental to define a model that can describe the properties of an integrating sphere. Resulting in a radiometric model of the sphere, which allows to determine the order of magnitude of the attenuation and the uniformity thus obtained.

Several Monte Carlo methods were studied bibliographically, however, it was verified that they were complex and very time consuming, resulting in an accuracy that was not required for this application. In order to create a simplified model, equations and the calibrated tables of irradiance uniformity and radiance sphere were used by the manufacture of integrating spheres, Labsphere[1].

Another important goal the main goals was to characterize the integrating spheres experimentally, so as to validate the selected model.

Several step-ups and experimental tests were performed that it allowed to verify and characterize the behaviour of integrating spheres in terms of uniformity, radiance, influence of the incident angle of the source, influence of the incident f-number of the source, and varying the distance from the detector to the sphere.

Overall, the experimental results demonstrate that the simplified model is valid for the intended application, with an accuracy of 10% for the uniformity, and the tests validated the use of an integrating sphere for astronomical spectrography.

Keywords: integrating spheres, radiometry, optical instrumentation

Resumo

A instrumentação para astronomia é uma das áreas onde a ótica teve uma evolução considerável nos últimos anos, e a observação espectroscópica de objectos astronómicos é um dos temas-chave. O objectivo desta tese é o estudo de esferas integradoras, no âmbito da instrumentação astronómica, para permitir a integração da luz solar para posterior injecção num espectrógrafo, através de uma fibra óptica. Para este estudo, é fundamental definir um modelo que possa descrever as propriedades e a esfera integradora.

Uma esfera integradora consiste numa estrutura esférica oca, coberta no seu interior por um revestimento refletor, tendo entre duas a três pequenas aberturas. Estas aberturas são denominadas por "portos de abertura", e dependem da utilização específica da esfera. Quando uma esfera oca é injetada com radiação eletromagnética, esta sofre várias reflexões pelas paredes difusas. Estas paredes são superfícies Lambertianas, o que produz uma irradiância e radiância uniformes nas paredes da esfera, uma vez que o feixe, ao incidir nas superfícies desta, se torna totalmente difuso e deixa de ter uma direção definida. A função de uma esfera integradora é, passando a redundância, integrar espacialmente o fluxo incidente. Este fluxo pode ser determinado através de um fotodetector, na saída da esfera.

Foi feito um estudo bibliográfico de vários modelos do Método Monte Carlo, que modelam esferas integradoras para várias situações, mas, uma vez que esses modelos são para situações em que o rigor é imprescindível, o processo seria demasiado demorado e complexo para o que era pretendido atingir. Mais concretamente, como se pretende criar um modelo simples e direto, que seja comprovável em contexto experimental, os modelos do Método Monte Carlo vão contra o objetivo deste trabalho.

Para a aplicação astronómica, é importante ter um modelo radiométrico da esfera, que permita ter uma noção da ordem de grandeza da atenuação e da uniformidade obtida com a mesma. Isto tendo em conta que o instrumento pode sempre ajustar-se, desde que o erro se encontre dentro dessa gama. Um dos objetivos principais será portanto caracterizar as esferas integradoras experimentalmente, de forma a validar o modelo simplificado.

Foram escolhidas três esferas. Uma esfera da International Light Technologies, com 25 cm de diâmetro, uma esfera da Thorlabs, com $5,08$ cm de diâmetro, e a última esfera, que não se trata de uma esfera integradora "comercial", mas sim de um globo revestido por dentro com tinta mate de forma a recriar, de uma forma algo rústica, barata e artesanal, uma esfera integradora com 25 cm de diâmetro. Esta última foi construída com o propósito de comparar os resultados obtidos aos resultados conseguidos com as outras duas mencionadas atrás. Cada esfera tem três aberturas, sendo que uma está definida como sendo o porto de entrada, que será onde a fonte de luz é injetada, e as outras serão os portos saída. A cada um destes portos está associado um detector próprio.

Como será necessário utilizar equipamento de dimensão pequena, pelo menos até 100 mm, não convém que a esfera ultrapasse essa dimensão, de forma a integrar a uma distância curta do foco do telescópio. A esfera da International Light Technologies é denominada esfera de referência, e a esfera da Thorlabs será então comparada com a de referência, visto que a esfera da Thorlabs corresponde às dimensões da aplicação.

O sistema utilizado para a medição consistiu em duas mesas, cada uma com um eixo de translação, conectadas entre si, acoplado às quais estava um detetor, a que chamámos detetor A. Os detetores (acima mencionados para os portos saída), são iguais. No entanto, o detetor A tem

uma área activa menor quando comparada relativamente à do outro detetor, a que chamámos detetor B. Isto deve-se ao facto de que o detetor B irá servir como detetor de referência. O detetor A, em conjunto com as mesas de translação, vai mover-se ao longo do porto de forma sistemática. Esse movimento foi programado em LabVIEW, e consiste em fazer com que o detetor A percorra uma matriz NxN, medindo várias vezes na mesma posição, e em todos os pontos da matriz, que estão separados por um pequeno intervalo, devolvendo o valor médio de cada posição (x, y) em que mede. Já o detetor B, enquanto o detetor A estiver em movimento, estará parado no seu porto, a manter a referência. Assim, a cada medição este valor de referência vai atenuar os valores obtidos pelo detetor A.

O modelo simplificado tem em consideração as equações de radiância, bem como da uniformidade da irradiância específicas da esfera. Estas foram retiradas do artigo de fabricante da Labsphere[1]. Neste trabalho, a tabela de uniformidade do fabricante foi usada como referência, para a comparação de resultados experimentais. Foi também utilizada para a interpolação de resultados para a uniformidade teórica, de acordo com as distâncias escolhidas.

Foram usadas três fontes de luz diferentes, a fonte de luz branca que cobre o espectro vísivel, a fonte de luz azul, com $\lambda = 375$ nm, e a fonte de luz vermelha, com $\lambda = 660$ nm. Foram realizados testes diferentes para determinar a uniformidade experimental e a irradiância experimental para cada esfera; Foi observada a resposta espectral da esfera da Thorlabs.

Para determinar a uniformidade experimental, foram efetuados os seguintes testes para cada esfera. Primeiro, tendo apenas a fonte de luz branca a incidir na esfera, foi afastado, para várias distâncias, o detetor A da esfera, de forma a recriar uma tabela de uniformidade. No segundo caso foram utilizadas ora apenas a fonte de luz azul, ora apenas a fonte de luz vermelha a incidir na esfera. Este teste foi apenas efetuado para uma distância do detetor à esfera. No terceiro caso, apenas realizado com a esfera de referência, e mais uma vez para uma só distância, foi testada a sensibilidade da injeção da fonte de luz branca, com várias posições e ângulos no porto de entrada. No último caso, foi testada a sensibilidade do número de abertura da fonte de luz, com a esfera da Thorlabs, e novamente para várias distâncias. Para cada teste foi calculada a uniformidade, para cada distância relativamente à esfera, e para cada fração do diâmetro do objecto, a dividir pelo diâmetro do porto.

Para calcular a irradiância experimental utilizou-se um radiómetro para medir a taxa de transferência de cada esfera integradora, para cada fonte de luz. Este teste foi realizado várias vezes, por forma a obter uma maior repetibilidade. Para obter a esposta espectral, utilizou-se um espectroradiómetro para medir à saída da esfera da Thorlabs, quando a fonte de luz branca era injectada.

Os resultados experimentais obtidos, relativos à uniformidade, estão dentro do esperado. Para menos de dois terços do tamanho do objecto em relação ao porto, a variação máxima é de 5%, para todas as esferas, e essa variação diminui à medida que o detetor se afasta da esfera. Como, para esta aplicação, há uma maior preocupação com as medições na parte vísivel do espectro, o teste com as diferentes fontes monocromáticas só demonstrou que não existe grande variação de uniformidade para um terço do diâmetro do porto. A sensibilidade da esfera para a variação da fonte de luz, para vários ângulos e posições, não é pertinente, existindo uma só variação, de até 3% no máximo, entre si. Alterando os números de abertura da fonte de luz para a mesma distância, e variando o número de abertura da fonte, não foi detetada qualquer variação apreciável entre estes para várias distâncias. A maior variação apresentou-se para um diâmetro de mais de dois terços do porto.

Os resultados da irradiância experimental demonstram que as esferas correspondem a cerca de 30% do modelo teórico. Obviamente que este modelo, sendo simples e otimista, não tem em conta os vários aspectos que fazem reduzir a taxa de transferência. E, futuramente, tem que se ter em conta esta variação. Analisando a razão da resposta espectral da esfera da Thorlabs com a fonte de luz branca, confirma-se de facto que, para a parte visível do espectro, a reflectância experimental é semelhante à do fabricante.

Palavras-chave: esfera integradora, radiometria, instrumentação ótica

Contents

List of Figures

List of Tables

Nomenclature

Greek symbols

Ω	Projected solid angle
Φ_i	Input flux.
π	Total projected solid angle from the surface.
ρ	Reflectance.

Roman symbols

A_e	Area of the exit port.
A_i	Area of the input port.
A_S	Surface area of the entire sphere.
D	Port Diameter
d	Object Diameter
E_e/E_o	Irradiance Uniformity.
E_S	Irradiance of the sphere
f	Port fraction.
l	Distance from the port to the detector.
L_S	Radiance of the sphere.
M	Sphere multiplier.
x	Distance from the source.

Chapter 1

Introduction

The motivation for this thesis was to study the radiometric model of an integrating sphere (IS). This radiometric model would be simple, but it would cover the uniformity and homogeneity of the IS and all the light's properties at the exit port of the integrating sphere. This integrating sphere will be used in an instrument coupled to a telescope and the model will be able to make measurements with an accuracy of an error of 10% or 20%, such accuracy is fairly standard for this type of characterization.

There are complex models[2][3], normally used in the metrology area where the IS are used and require tolerances much tighter; those models normally are Monte Carlo Methods. It was made a bibliographic study of some models, and it was verified that there was an increased complexity associated with them. Implementing those models would be very difficult and also challenging to validate experimentally. In this work, experimental validation is fundamental. The idea is to work with a type of spheres that are not a perfect model, are smaller than what is usually used in metrology and are not spheres used in the mentioned models.

An integrating sphere is an optical component that has a hollow spherical cavity with a few openings, that are designed as the ports; these can be the entrance, exit, calibration, or the user's port. It depends on what the sphere is designed for. An integrating sphere collects electromagnetic radiation from an external source into the optical device, usually for flux measurement or for optical uniformity. The interior cavity is painted with a reflective or diffuse material, so that when the radiation is introduced into the integration sphere, it strikes the reflective walls and undergoes multiple diffuse reflections. After that, the radiation is dispersed in a highly uniform state on the sphere's walls. The function of an integrating sphere is to spatially integrate radiant flux, which can then be measured using a detector.[1] The use can be simple, to homogenize or integrate light, which is the application in this work. There are different sizes, it can go from 25mm to $2,5$m, figures 1.1 and 1.2.

Figure 1.1: Image of an example of a small integrating sphere is this model 819D-SL-2 from *Newport*. An IS with 3 ports, a diameter of $5cm$ (PTFE).[4]

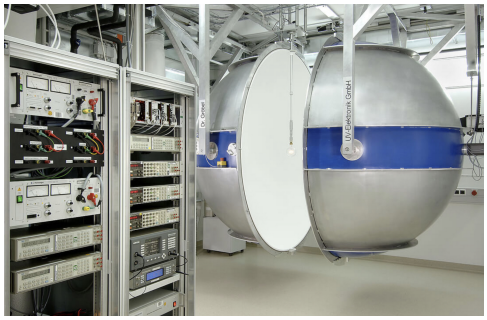

Figure 1.2: Image of an example of a big integrating sphere is this model BASO4 from *Opsytec Dr. Gröbel*. An IS with 2 ports, a diameter of $2,5m$ (BASO4).[5]

The first thing that was done at the beginning of this thesis was to implement the Monte Carlo models, and it was concluded that those models were complex and cumbersome: the process of understanding, the development, the outlining, and alterations for the objectives set to this work on different aspects. These works are really good and are normally associated with applications where conditions are required to have a better accuracy (10%), which was not intended in this work. The solution to this would be to focus on a simplified model.

The work described in this thesis is intended as simple application to study the light that comes from the sun. The sun, as a star model, can be use as a proxy to discover new stars and consequently new solar systems similar to ours. Nowadays, studies of the Sun have gained momentum as the scientific community turns toward the study and discovery of exoplanets[6]. For example, HELIOS (HARPS Experiment for Light Integrated Over the Sun) is a solar telescope feeding the HARPS (High Accuracy Radial Velocity Planet Searcher) instrument, which is attached to the ESO 3.6-metre telescope[7]. HARPS is one of the most powerful planet hunters in existence and spends most nights monitoring stars for minute signals that indicate the presence of an exoplanet[7]. HELIOS will be able to feed sunlight into HARPS to achieve very high-precision spectroscopy of the Sun for several hours per day. In addition to learning about the Sun itself and in particular improving our understanding of stellar activity, the HELIOS project will lead to an improvement of exoplanet detection techniques[7].

Another instrument that is currently being developed is the PoET (Paranal solar Espresso Telescope)[6]. ESPRESSO (Echelle SPectrograph for Rocky Exoplanets and Stable Spectroscopic Observations)[8] was designed as a highly stable fiber-fed échelle spectrograph which may simultaneously receive light from one or up to four Unit Telescopes (UTs) of the VLT. The preliminary design concept of PoET is a two-telescope mount: The pointing telescope is used to get an image of the full disk of the Sun, while the main/guiding telescope, with its higher resolution, can spatially resolve a smaller area in higher detail. It is expected that with this configuration, images of the Sun's surface can be obtained with a spatial resolution better than 1 arc second[6].

The motivation of this thesis is to design an instrument based on a telescope that will be connected by fiber to a spectrograph; therefore it's the necessity of understanding the behaviour of an integrating sphere when observing an extensive object who that possesses structures of interest to develop further studies. The sun, our nearest star is a complex system capable of producing many phenomenons which are rapidly becoming the focus of the scientific community,

such as sunspots or solar flares . In a telescope, the light collected from the sun, uniform and homogenize by the IS, can be made to be incident into a punctual object in the fiber optic. The latter is connected with a spectrograph, which will interpret the incoming light. A spectrograph is an instrument that separates incoming light by its wavelength or frequency and records the resulting spectrum in some kind of multichannel detector, like a photographic plate.[9] The examples presented before have a spectrograph implemented.

1.1 Objectives and Approaches

The objective of this work is to develop a simplified model using the equations that rule the integrating sphere and to study, test, and validate that model in terms of uniformity. The development of a complex model such as the Monte Carlo method falls outside of the scope of the thesis since the tolerance is not fundamental.

This objective will be approached in the following way. Chapter one has the work introduction: the background is presented followed with examples and current work, and the motivation of this work is clarified.

Chapter two has modeling the integrating sphere: the Monte Carlo models that were studied are provided; and the simplified model with the corresponding equations are explained.

Chapter three has the experimental characterization: all the experimental work will be described in order to characterise the integrating sphere with the objective to validate the simplified model and characterise which level of accuracy this method has.

Chapter four has the experimental results: an example of how the collected data is analyzed is demonstrated, and the experimental results for each test is presented with the respective conclusions.

Chapter five has the recap of the objectives of this thesis and the description of the experimental tests; has the conclusions for each test, the final conclusions and suggestions for future work.

Chapter 2

Modeling the Integrating Sphere

2.1 Monte Carlo Methods

As mentioned before, Monte Carlo methods fall outside of the scope set for this thesis. However, for comparison purposes, it is worth mentioning a few studies as a reference for this type of procedure.

The complex models that were studied were *The design, construction, and calibration of a spectral diffuse/global irradiance meter*[2] and *Computer modeling of integrating spheres* [10] from Blake G. Crowther; and *Monte Carlo modeling of an integrating sphere reflectometer*[3], and *Numerical modeling of an integrating sphere radiation source*[11] from Alexander V. Prokhorov. All of these models has an uncertainty in the range of $0,1\%$ to 1%

2.2 Simplified model

The goal behind this chapter is to use the general theoretical notions for the purpose of simplifying while achieving results with an acceptable tolerance.

Integrating spheres produce illumination that has extremely uniform radiance and irradiance. An integrating sphere is a hollow spherical shell coated on the inside with a highly reflecting diffuse coating. The projected solid angle from any point on a sphere to any element of area on the sphere is the same, regardless of location. This fact combined with the diffuse coating and the multiple reflections cause any light introduced into the sphere to produce uniform irradiance and radiance on the wall of the sphere. A hole or 'port' in the sphere allows this uniform illumination to be used in an optical system. [12]

2.2.1 Radiation exchange within diffuse surfaces

Having two diffuse surface, figure 2.1, they can be described succinctly by the differential form of the equation of radioactive transfer.

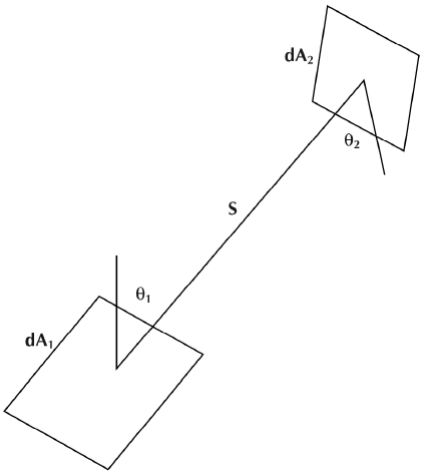

Figure 2.1: Radiation exchange between two differential elements of diffuse surfaces.[1]

$$dF_{d1-d2} = \frac{\cos\theta_1 \cos\theta_2}{\pi S^2} dA_2 \tag{2.1}$$

where the fraction of energy leaving dA_1 and arriving at dA_2 is known as the exchange factor dF_{d1-d2}. The angles θ_1 and θ_2 are measured from the surface normals.

If coating the inside of a sphere with a type of diffusive surface, figure 2.2.

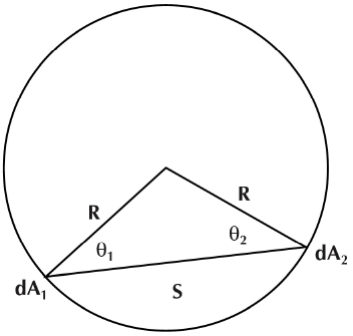

Figure 2.2: Radiation exchange between two differential elements inside of an diffuse surface sphere.[1]

The distance S is the same as from θ_1 and θ_2, hence $S = 2R\cos\theta_1 = 2R\cos\theta_2$. So, equation 2.1 becomes:

$$dF_{d1-d2} = \frac{dA_2}{4\pi R^2} \tag{2.2}$$

Since it is independent of viewing angle and the distance between the areas, the result is relevant. For this reason, the fraction of flux received by dA_2 is the same for any radiating point on the surface. So, if the infinitesimal area dA_1 instead exchanges radiation with a finite area A_2 and because the result is also independent of dA_1, then the equation 2.2 becomes:

$$dF_{d1-d2} = \frac{1}{4\pi R^2} \int_{A_2} dA_2 = \frac{A_2}{4\pi R^2} \Longrightarrow F_{1-2} = \frac{A_2}{4\pi R^2} = \frac{A_2}{A_S} \tag{2.3}$$

where A_S is the surface area of the entire sphere. Hence, the fraction of radiant flux received by A_2 is the fractional surface area it occupy within the sphere. [1][13][14][15][16]

2.2.2 The integrating sphere radiance equation

Radiance indicates how much of the power emitted or the amount of flux collected by an emitting or reflecting surface will be received by an optical system looking at the surface from some angle of view - the solid angle subtended by the optical system's aperture.

If light incident on a diffuse surface creates a virtual light source by reflection, the light emanating from the surface is best described by its radiance, L, the flux density per unit solid angle, $(W/m^2/sr)$,

$$L = \frac{\Phi_i \rho}{\pi A} \tag{2.4}$$

where ρ is the reflectance, A is the illuminated area, and π the total projected solid angle from the surface.

To describe the radiance of an internally illuminated integrating sphere, the equation must consider both multiple surface reflections and losses through the port openings needed to admit the input flux and view the resulting radiance. Taking into account a sphere with input port area A_i and exit port A_e, figure 2.3, the input flux is perfectly diffused by the initial reflection.

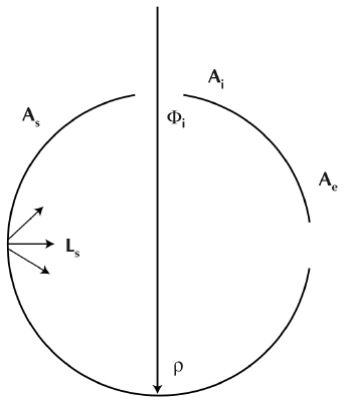

Figure 2.3: An integrating sphere with a input flux Φ_i, input port area A_i and exit port A_e.[1]

The amount of flux incident on the entire sphere surface will be $\Phi_i \rho(\frac{A_S - A_i - A_e}{A_S})$. The quantity in parentheses denotes the fraction of flux received by the sphere surface that is lost by the port openings. It is better to write in terms of $(1 - f)$ where f is the port fraction and $f = \frac{A_i + A_e}{A_S}$. If there are more than two ports, then f is calculated from the sum of all port areas.

It must be taken into consideration, the reflections inside of the sphere. If the amount of flux incident on the sphere surface after the second and third reflection are, respectively, $\Phi_i \rho^2 (1 - f)^2$ and $\Phi_i \rho^3 (1 - f)^3$. For n reflections, the total flux incident over the entire surface of the integrating sphere will be $\Phi_i \rho (1 - f) 1 + \rho(1 - f) + ... + \rho^{n-1}(1 - f)^{n-1}$. If it is expanded to an infinite power series and since $\rho(1 - f) < 1$, the total incident flux (in Watts) is reduced to

$$\frac{\Phi_i \rho (1 - f)}{1 - \rho(1 - f)} \tag{2.5}$$

With that conclusion, the total flux incident of the sphere surface is higher than the input flux because of multiple reflections inside the sphere.

With equations 2.4 and 2.5, the surface radiance of the sphere will be:

$$L_S = \frac{\Phi_i}{\pi A_S(1-f)} \cdot \frac{\rho(1-f)}{1-\rho(1-f)} = \frac{\Phi_i}{\pi A_S} \cdot \frac{\rho}{1-\rho(1-f)} \tag{2.6}$$

The equation is used to predict the integrating sphere radiance for a given input flux as a function of sphere diameter, reflectance, and port fraction. Although the radiance decreases as sphere diameter increases. [1][13][14][15][17]

2.2.3 The sphere multiplier and the average reflectance

From the previous subsection, the multiple reflections inside the sphere are referred on the second part of the equation 2.6, it has an unitless quantity which is called the sphere multiplier:

$$M = \frac{\rho}{1-\rho(1-f)} \tag{2.7}$$

But equation 2.7 is for the case where incident flux affects the wall of the sphere, the reflectance of the wall is uniform, and the reflectance of all the ports areas is zero. The general expression is

$$M = \frac{\rho_o}{1-\rho_w(1-\sum_{i=0}^{n} f_i) - \sum_{i=0}^{n} \rho_i f_i} = \frac{\rho_o}{1-\overline{\rho}} \tag{2.8}$$

where ρ_o is the initial reflectance for incident flux; ρ_w is the reflectance of the sphere wall; ρ_i is the reflectance of the coating when the port opening i is closed; f_i is fractional; and finally $\overline{\rho}$ is the average reflectance for the entire integrating sphere. [1][14][15][18]

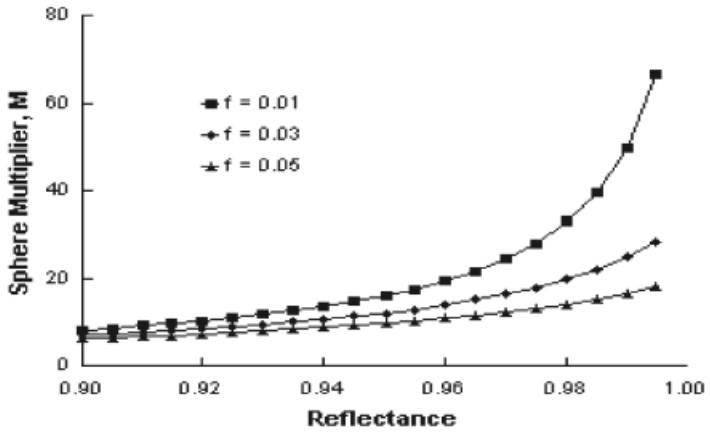

Figure 2.4: Sphere multiplier in function of the reflectance of the integrating sphere.[1]

2.3 Design parameters

Using an integrating sphere for any application requires taking some considerations for the parameters. It goes from the optimum sphere diameter based on the number and size of port openings, to selecting the proper sphere coating considering the spectral range as well as the performance required. Even the use of baffles are in consideration.

The work on this thesis was developed with IS diameters from $5cm$ to $25cm$, with no baffles and an output with no fibers. The characterization of the exit port is necessary before an implementation with a fiber can be studied - this study was not conducted on this thesis. The

application of a fiber to the exit port is a trivial procedure and the resulting output should depend only on the fiber characteristics. It is recommended that a setup linking a sphere to a fiber undergoes additional irradiance studies in order to accommodate and adapt the resulting data described in this thesis to this additional optical component.

2.3.1 Integrating Sphere Diameter

Figure 2.4, shows that decreasing the port fraction has a dramatic effect on increasing the sphere multiplier. Therefore, no more than 5% of the area of the integrating sphere can be consumed by the port openings.

The integrated spheres are designed by initially considering the diameter required for the port openings. The port diameter is driven by both the size of devices as well as the geometrical constraints required by a sphere system.

In general, a small sphere produces a higher radiance. However, since the integrating sphere is usually used for its ability to spatially integrate input flux, a larger sphere diameter with smaller port fraction is a better choice. However, if the integrating spheres have a high reflectance material, it can optimize spatial performance. [1][18]

2.3.2 Irradiance Uniformity

Any surface, real or imaginary, whose radiance is independent of direction is said to be a Lambertian radiator, mainly because it obeys Lambert's cosine law, which is that the irradiance from an element of area in the surface varies as the cosine of the angle θ between that direction and the perpendicular to the surface element[19][13][20]:

$$E(\theta) = E(0)\cos\theta \tag{2.9}$$

Radiance is the flux density leaving a radiant surface as viewed from a distance away from the surface. If the integrating sphere has a Lambertian surface, it features a perfectly diffuse radiance, independent of the viewing angle. Irradiance is the flux density that falls on a surface and is measured in the plane of the surface.

Since the integrating spheres are mostly used to test an imaging system, it is desired that a uniform radiance within the field of view is achieved for the system under test. If it is used to test a nonimaging system –, then the desired effect is uniform irradiance, and the device under test is, at some distance of the port, placed coaxial with the sphere. When this happens, two important quantities are to be determined. The axial irradiance at the center of the object and the irradiance at the off-axis edge.

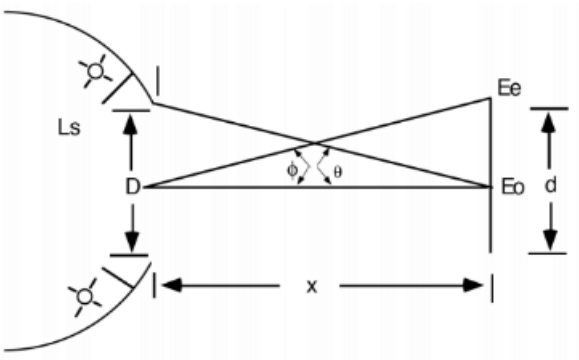

Figure 2.5: Scheme to determine the uniformity. [1]

Considering figure 2.5, the axial illuminance, E_o, is given by,[1]:

$$E_o = \pi L_S \sin^2 \theta \tag{2.10}$$

Even for a perfectly Lambertian, the uniformity of the irradiance across a plane object at a finite distance will vary with the angle of the off-axis θ. The uniformity is defined as the ration of the irradiance at the edge of the object to the axial irradiance, E_e/E_o.

Irradiance Uniformity (Ee/Eo)
Distance from Source (x/D)

Object Diameter d/D	0.00	0.10	0.20	0.25	0.50	0.75	1.00	1.50	2.00	2.50	3.00	5.00	10.00
0.1	1.00	1.00	1.00	1.00	1.00	1.00	1.00	1.00	1.00	1.00	1.00	1.00	1.00
0.2	1.00	1.00	0.99	0.99	0.98	0.98	0.99	0.99	1.00	1.00	1.00	1.00	1.00
0.3	1.00	0.99	0.98	0.97	0.96	0.96	0.97	0.98	0.99	0.99	1.00	1.00	1.00
0.4	1.00	0.99	0.96	0.94	0.92	0.93	0.95	0.97	0.98	0.99	0.99	1.00	1.00
0.5	1.00	0.97	0.92	0.90	0.88	0.90	0.92	0.96	0.97	0.98	0.99	1.00	1.00
0.6	1.00	0.95	0.88	0.85	0.82	0.86	0.89	0.94	0.96	0.97	0.98	0.99	1.00
0.7	1.00	0.92	0.81	0.78	0.76	0.81	0.86	0.92	0.95	0.96	0.97	0.99	1.00
0.8	1.00	0.84	0.72	0.69	0.70	0.76	0.82	0.89	0.93	0.95	0.97	0.99	1.00
0.9	1.00	0.70	0.60	0.59	0.62	0.71	0.78	0.87	0.92	0.94	0.96	0.98	1.00
$\sin^2\theta$	1.000	0.962	0.862	0.800	0.500	0.308	0.200	0.100	0.059	0.038	0.027	0.010	0.002
$\pi\sin^2\theta$	3.142	3.021	3.708	2.513	1.571	0.967	0.628	0.314	0.185	0.121	0.085	0.031	0.008

Note: Boundary lines delineate regions of 98%, 95%, and 90% irradiance uniformity

Figure 2.6: The uniformity is determined as both the distance and the dimension of the object are expressed as multiples of the sphere port diameter, x/D and d/D respectively. [1]

Analysing fig 2.6, the uniformity is 100% at the plane of the port, and it decreases as the object is moved away from it for a short distance and improves as the distance becomes sufficiently long. Transforming the values in Fig. 2.6 into a graphic, we have Fig. 2.7.

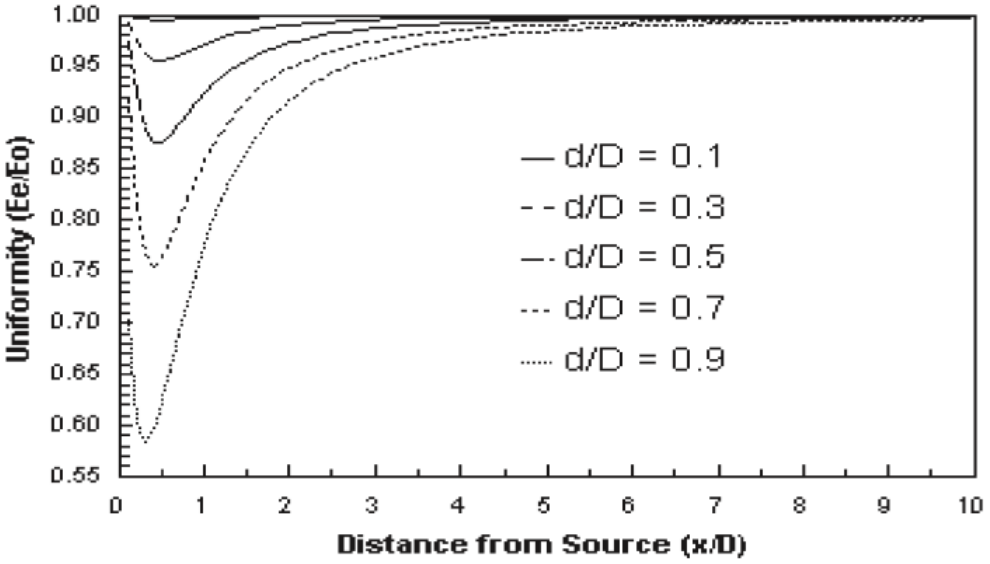

Figure 2.7: Figure 2.6 represented as a graphic. [1]

Figures 2.6 and 2.7 are based on theoretically calculated uniformity values for the perfect ideal Lambertian source. For laboratory measurements of real integrating sphere sources correlate extremely well with these predicted values. Therefore, the data provided can be used as design guidelines to choose the correct uniform source for a particular application. [1]

Therefore, in this thesis, all the experimental uniformity results will be compared to the fig 2.6.

Chapter 3

Experimental Characterization

In this chapter, all the experimental work will be described in order to characterise the integrating sphere with the objective to validate the simplified model - that use the formulae described in section 2.2 - and characterise which level of accuracy this method has.

3.1 Experimental Set-Up

Before characterising the experimental tests, it is necessary to explain the experimental set-up with the following components.

3.1.1 Integrating Spheres

In this thesis, it was used three different spheres. The first and big sphere was an INS250 Integrating Sphere from the International Light Technologies [21], fig 3.1; the second and smallest sphere was an IS200 series, ∅2", from Thorlabs [22], fig 3.2; and the last *sphere* it was a globe, fig 3.3.

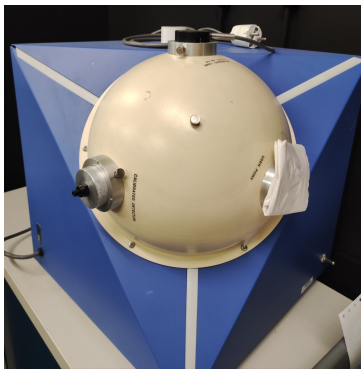

Figure 3.1: Photograph of the Big Sphere: INS250 Integrating Sphere from the International Light Technologies[21], used in this work.

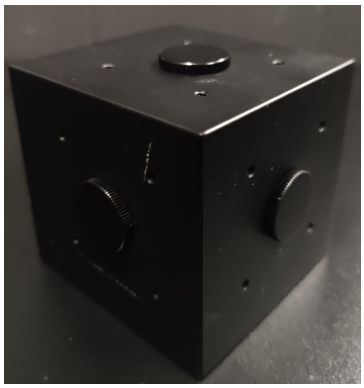

Figure 3.2: Photograph of the Small Sphere: IS200 series, ∅2", from Thorlabs [22], used in this work.

Figure 3.3: Photograph of the Globe used in this work.

	Sphere Diameter (mm)	Port Diameter (mm)	Port Width (mm)	Sphere Reflectance (@350 to 1500nm)
Big Sphere (INS250)	250	37,6	12,3	98,5%
Small Sphere (Thorlabs)	50,8	12,7	3,5	99%
Globe	251	30	2,7	Unknown

Table 3.1: Characterization of the integrating spheres from their respective technical sheets [21][22] except the globe.

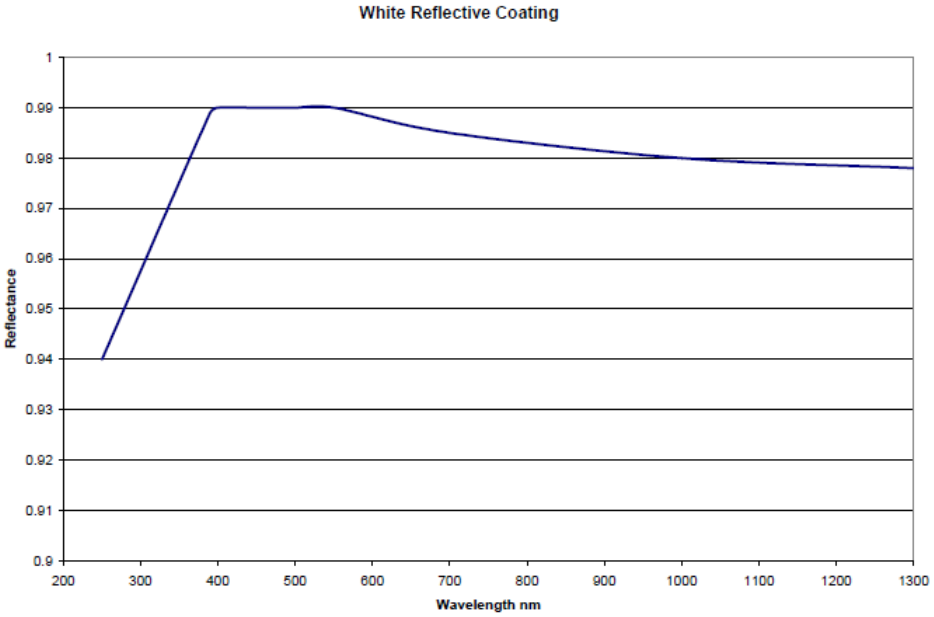

Figure 3.4: Plot showing white reflective coating of the INS250 integrating sphere[21].

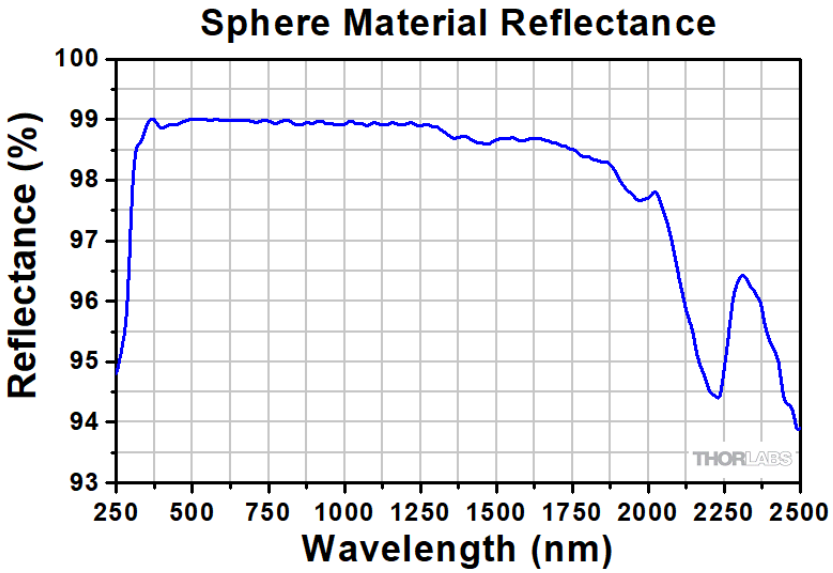

Figure 3.5: Plot showing sphere material reflectance of the Thorlabs integrating sphere[22].

The INS250 sphere - that will be called Big Sphere or BS from now on - would serve as a

reference, it was too big for what this work requires. But this sphere has features that makes it the sphere reference, it is a good example to validate the model and also impose limits for the desirable dimension. The Thorlabs sphere - that will be called Small Sphere or SS - was a recent sphere and more ideal for this work.

It's important to enhance that the BS has two decades whereas the SS has fewer years. The use and wearing of the material are great factors that will reduce the reflectance over time. Even though it was specified in table 3.1, it is not guaranteed it was still the same.

The globe was a rustic and simple attempt to recreate an integrating sphere. The globe was painted with matte white, with the objective to understand how the homogeneity work. Even though the reflectance is unknown, it can be calculated -in order of magnitude- comparing with the BS since they are similar. The purpose of this sphere was a recreation of an IS, 'with the same features', simple and cheap, and in the future, it could be use in practical classes.

All these spheres have three ports and no baffles inside.

3.1.2 Light Sources

In this work it was used three light sources, to study the sphere sensibility to the light injection. The first light source was a white light from LaboControle, Olympus Europe, Highlight 3100, fig 3.6. This light source uses a projector lamp, tungsten halogen, from Sylvania, of $21V$ and $150W$, fig 3.7. This light source has a bundle of fibers at the exit with a $NA = 1,37$, and the halogen bulb covers all the visible spectrum, $380nm$ to $700nm$.

The second light source was a M375SF2 from Thorlabs, fig 3.9, is a Fiber-Coupled High-Power LED with a nominal wavelength of $375nm$, outputs more than $3,2mW$ of power, and is mounted to the end of a heat sink. The output is compatible with SMA fiber connectors and has the spectrum presented in fig 3.10 [23].

The third light source was a M660FP1 from Thorlabs, fig 3.11, is a Fiber-Coupled LED with a nominal wavelength of $660nm$, outputs more than $10,6mW$ of power, and is mounted to the end of a heat sink. The output is compatible with SMA fiber connectors and has the spectrum presented in fig 3.12 [24].

To be able to use the last two light sources, it was used a M28L01 fiber[25], $NA = 0,39$, $\varnothing = 400\mu m$, SMA-SMA Fiber Patch Cable, Low OH, from Thorlabs. This fiber has the attenuation shown in fig 3.13.

Figure 3.6: Photograph of the white light source, Olympus Highlight 3100 from Labo-Controle

Figure 3.7: Photograph of the tungsten halogen bulb from Sylvania.

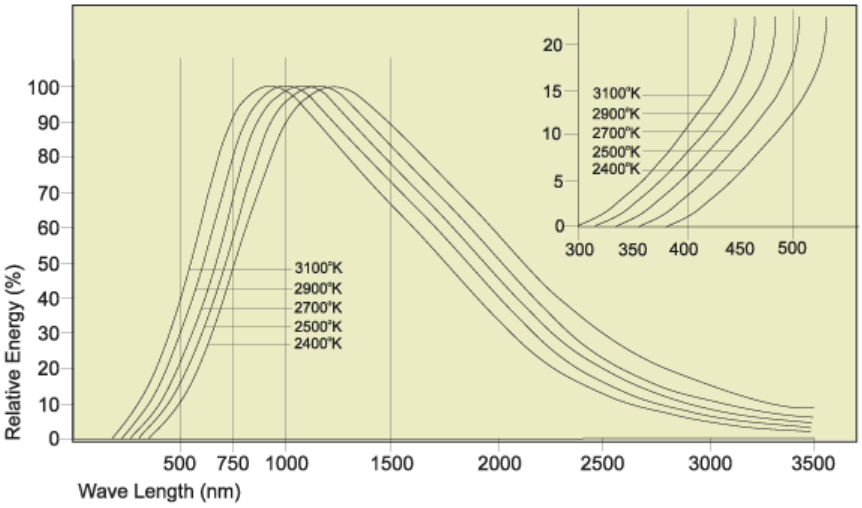

Figure 3.8: Plot of the spectral radiation output for tungsten filament lamps.[26]

Figure 3.9: Image of the M375SF2 Fiber-Coupled High-Power LED from Thorlabs[23].

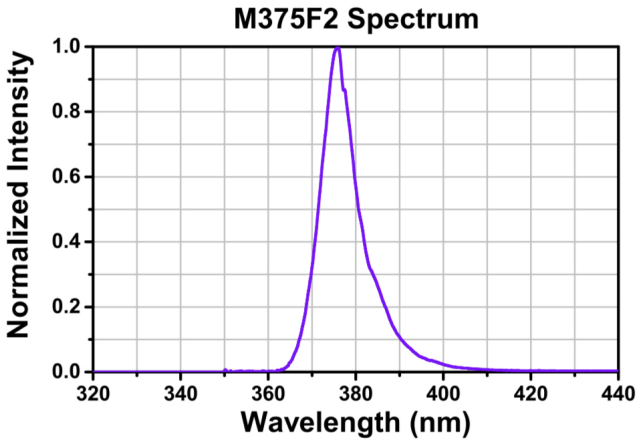

Figure 3.10: Plot of the M375SF2 Spectrum[23].

Figure 3.11: Image of the M660FP1 Fiber-Coupled LED from Thorlabs[24].

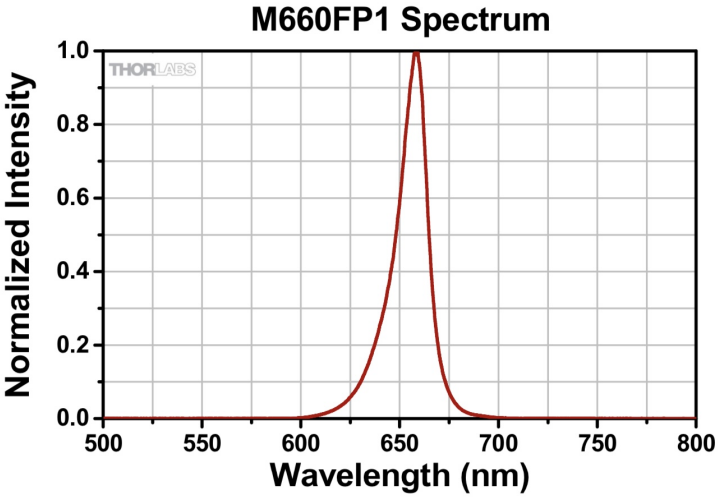

Figure 3.12: Plot of the M660FP1 Spectrum[24].

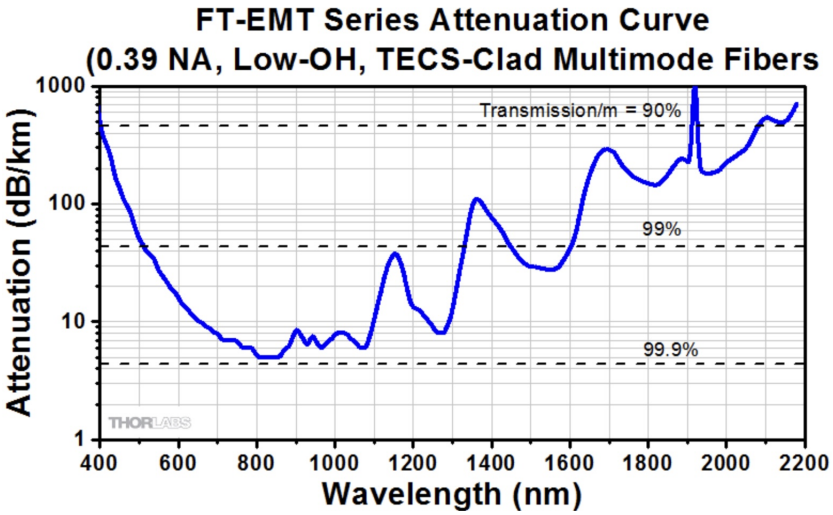

Figure 3.13: Plot of the M28L01 fiber attenuation curve[25].

3.1.3 Detectors

The uniformity was measured with the detectors PDA36A-EC Si amplified detectors from Thorlabs[27].

Since the integrating spheres have three ports, one is chosen the input port and the other two the exit ports with a respective detector. These detectors are the same except for the active area. One detector, called **detector B**, fig 3.14, has an active area of $A = 13mm^2$[27], and the other detector, **detector A**, fig 3.15, has an active area of $A = 0,79mm^2$, imposed using a diaphragm.

Figure 3.14: Photograph of the detector **B** with an active area of $A = 13mm^2$.

Figure 3.15: Photograph of the detector **A** with an active area of $A = 0,79mm^2$, created using a diaphragm.

These detectors are a good choice since they have a response curve, from $350nm$ to $1100nm$, that includes the three light sources, fig 3.16.

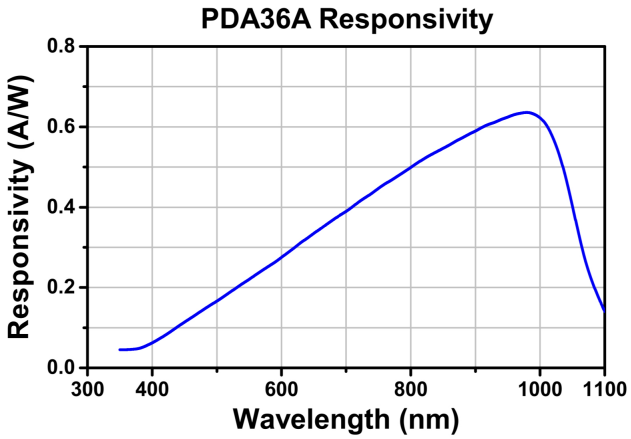

Figure 3.16: Plot of the PDA36A responsivity[27].

The set-up scheme of the detectors with the integrating sphere was the same for all the spheres. In figure 3.17, has the detector A represented by the movable detector and detector B by the fixed detector.

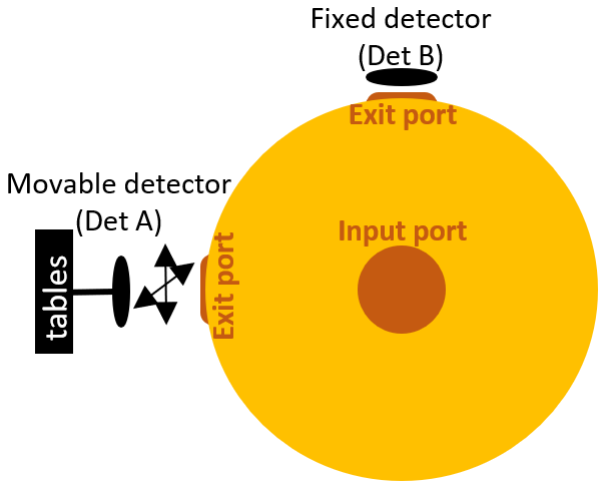

Figure 3.17: Schematization of the detectors with the integrating sphere. The yellow circle is the IS, the brown circles are the ports, the black rectangle is the tables and the little black circles are the detectors.

The detector A is the movable detector because this one will be linked with two one-axis translation tables, so it will allow the detector to scan the entire port; while the detector B will be fixed to the port, it will monitor possible variations and serve as a reference, like a control sampling.

3.1.4 Translation tables

Two one-axis translation tables were used with the detector A to capture all the light at the exit port. The tables are from Physik Instrumente, model $126K002$, with a range of 0 to $25mm$, fig 3.18. The tables were on top of each other, one table would make the movement in the horizontal axis and the other in the vertical axis, see figure 3.19.

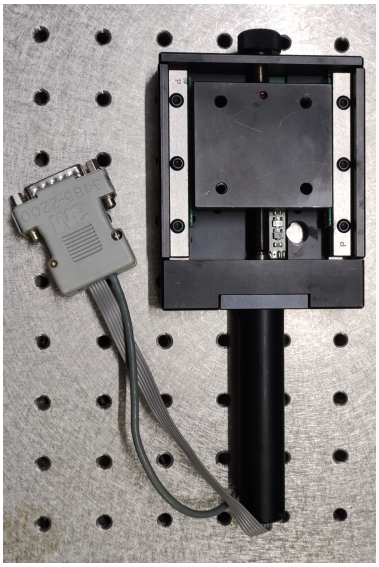

Figure 3.18: Photograph of the translation table from Physik Instrumente.

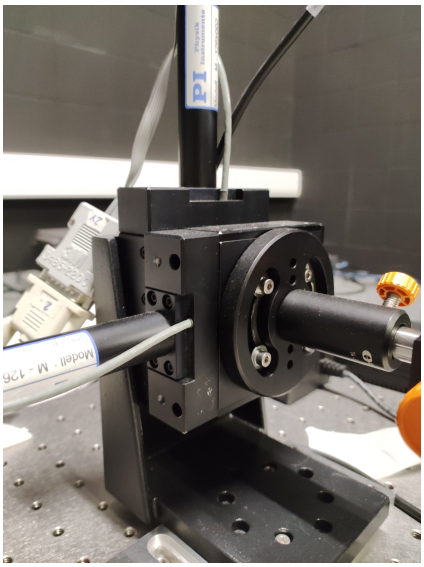

Figure 3.19: Photograph of the set-up in the laboratory: two one-axis translation tables linked with the detector A (who's hidden in the image).

It was programmed in LabVIEW a model into the tables so that they would make two paths: the direct and inverted path. The direct path is the red one: when it departs from initial position and ends at final position, and the detector will measure the light at the designed interval, or what it was called, the step, fig 3.20. The inverted path, in green, will depart from the final position to the initial, and the detector will measure the light at the same step, fig 3.21.

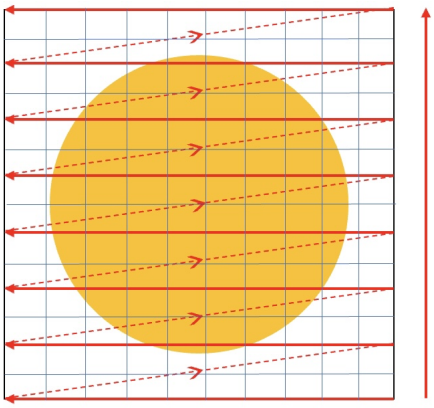

Figure 3.20: Image of the direct path made by the tables. The yellow circle is the port entrance.

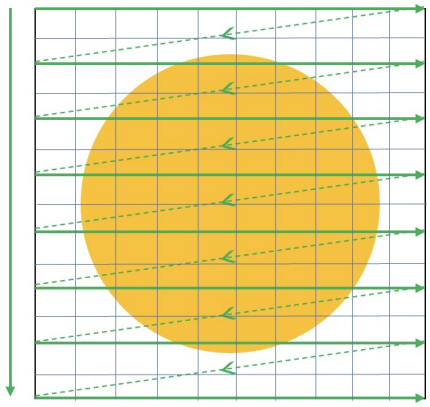

Figure 3.21: Image of the inverted path made by the tables. The yellow circle is the port entrance.

The paths were graphically programmed in LabVIEW and the figures are in the appendix **??**.

In fig A.1, it is shown the process of parking the tables, and it sends a message to the user where he decides if it wants to park or not the tables. The parking is the reassurance that the tables starts from $x = 0, y = 0$. This specific program of parking was constructed previously by the professor Alexandre Cabral. The rest of the program was created by Andreia Domingos.

Fig A.2 is where the direct movement happens. The number N indicates the dimension of the matrix and it is provided by the user. The i is the iteration. The number Step is also

provided by the user and indicates which points will be measured. The x_o and y_o indicate the coordinates where the measurement starts, and are themselves indicated by the user. For example, since the BS has a bigger port diameter than the range of the table, the start positions will be $x_o = 0, y_o = 0$. But the SS has a smaller port diameter, so the start positions will be $x_o = 5, y_o = 5$, since the measurements before that wouldn't matter. The input buffer size and scan rate can be provided by the user, but they were never actually altered: these two decide how long, and how many values, the detector will measure in that specific point. For example, the input buffer size is 25 and the scan rate is 10, so the detectors will measure 25 times in 10 seconds, so it takes $2,5$ times per second, in every point for every measurement, throughout the matrix. The distance along the axis is just an information for the user.

The function that makes the direct movement is the function of quotient and remainder. The iteration i will be divided by the number N. The matrix within which the system will move has a size NxN, and the iteration will run from 0 through to $NxN - 1$. The remainder $(x - y * floor(x/y))$ is multiplied by the Step, and this multiplication produces the x-axis. This information is sent to table #1, that makes the movement across the x-axis. Whereas the quotient $(floor(x/y))$, also multiplied by the Step, produces the y-axis. And this information is sent to table #2, which stays still until the table #1 arrives at the final position of the x-axis (or, equivalently, until the remainder reaches $N - 1$). After that, as i/N grows, the quotient goes to the next value in the y-axis, that is the table #2, and the table #1 goes back to the start. And so the table moves sequentially across the port until the end of the matrix. As shown in fig 3.20.

Figure A.3, it is shown the graphical program of the inverted path. The function that makes the inverted movement is the function of quotient and remainder, but difference is that, what is divided by N is $((NxN) - 1) - i$. The remainder, the table #1, starts at the end of the matrix, (N, N), while the table #2 is at the end of the matrix as well. And the tables moves in inverted way until they reach the origin, as shown in fig 3.21.

Figures A.4, A.5 and A.7 are related to each other and while the figures A.4 and A.5 shows the program in the direct movement cycle, but it is the same in the inverted cycle after fig A.3.

In fig A.4, the program will send the information to the user through the display, fig A.7. It has two waveform graphics, an array (array 0) with the values measured in every specific point from detector A, another array (array 1) with the values from detector B. Both arrays are linked at the end with a mean tool, and that mean value is sent to a waveform graphic as well.

Figure A.5, it is shown the graphical program that allows the information to be saved in an excel file. The information is: time, scan rate, input buffer size, position in x, position in y with the respective mean value 0 and mean value 1 for each position.

Figure A.6 it is shown the graphical program when it finishes running, and send the tables back to $(0, 0)$.

Figure A.7 is the user display: it shows the information inserted by the user in fig A.2; the respective graphics and the values of the arrays from fig A.4; and where the user can save the excel in the computer, fig A.5.

The information on the left side is the direct scan ('varrimento') and the right side is the inverted scan ('varrimento invertido'). What is edited by the user are the green and blue rectangles: the first being the name and the location of the excel file, the latter is the information shown in fig A.2.

As said before, with an input buffer of 25, the detectors measure 25 times in the same point.

So in the yellow rectangles, for their respective scans, the waveform graphs presents the 25 values for every position, while the plot 0 is the detector A and plot 1 is the detector B. The graphs resets at the end of the measurement in that point.

Inside of the red rectangles are the arrays and mean values for their respective scans: the first array shows the list of the 25 measured values and the respective mean value, for detector A and second array and mean value is for detector B.

And inside of the black rectangle is the waveform graph, for each scan, with the mean values along the axis, and it resets at the end of the measurement in that axis.

For a better description of the movements of the tables, the following example is provided. Since the BS has a port diameter of $37,6mm$, the following procedure was made:

1. The tables would be positioned at $(12,5; 12,5)$;

2. The center of the detector A would be positioned at the center of the port;

3. Since the range of the tables are smaller than the port diameter, the detector will measure from 0 to 25, included, on both axis;

4. With this sphere, it was designed a step of $1mm$.

5. After having the previously information, the program would start and park the tables at position $(0, 0)$.

6. The detector would measure (direct path) from $(0, 0)$, $(0, 1)$, $(0, 2)$ ... to $(0, 25)$, then it comes back to $(0, 0)$.

7. The table #2 goes up to $(1, 0)$ and table #1 continues, $(1, 1)$ ... $(1, 25)$. This process will be repeated until it reaches $(25, 25)$. The direct path, fig 3.20.

8. Once it reaches the position $(25, 25)$, it starts the inverted path, fig 3.21.

9. From $(25, 25)$ table #1 continues $(24, 25)$, $(23, 25)$ ... $(0, 25)$, and once it reaches $(0, 25)$, it goes back to $(25, 25)$. Table #2 comes down to $(25, 24)$.

10. The table #1 continues to make the inverted path until it reaches $(0, 0)$.

3.1.5 Powermeter

The Powermeter was used to determine the sphere throughput. It was used a Compact Photodiode Power Head with Silicon Detector: S120C from Thorlabs[28], fig 3.24.

The S120C power head is designed for general purpose optical power measurements. The high sensitive photodiode with large active area in combination with a reflective, diffused ND filter enables power measurements of $50nW$ to $50mW$ in free-space and fiber-based applications. With a wavelength range of 400 to $1100nm$, $9,7mm$x$9,7mm$ active detector area, $\varnothing 95mm$ for input aperture, and a response less than $1\mu s$, the responsivity is presented in fig 3.23[28].

Figure 3.22: Image of the compact Photodiode Power Head with Silicon Detector: S120C from Thorlabs[28].

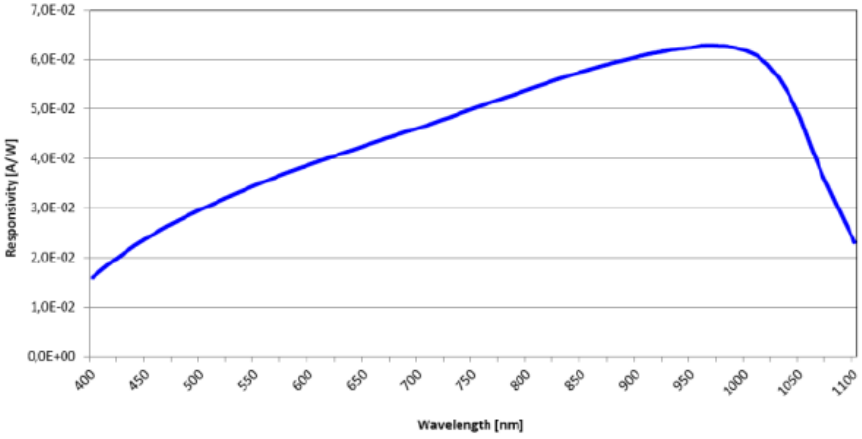

Figure 3.23: Plot of the responsivity of the Compact Photodiode Power Head with Silicon Detector: S120C[28].

3.1.6 Spectrometer

The spectrometer was used to test the spectral response of the integrating spheres. It was chosen the USB4000 Fiber Optic Spectrometer from Ocean Optics[29], fig 3.24.

The USB4000 Spectrometer has a detector 3648-element linear silicon CCD array, with a wavelength range of 200 to 1100nm, a fiber optic connection of SMA 905 to single-strand optical fiber, $NA = 0,22$, and an integration time of $3,8ms$ to $10s$[29].

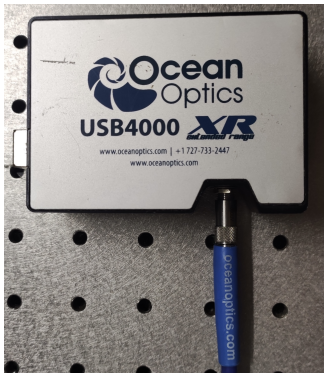

Figure 3.24: Photograph of the USB4000 Fiber Optic Spectrometer from Ocean Optics[29].

3.2 Characterization Tests

Different experiments tests were made to test the simplified model and the characterization of the integrating spheres. In tests A to D, the uniformity was measured with the detectors (subsec 3.1.3) and tables (subsec 3.1.4). The following tests will be described in their corresponding subsections.

3.2.1 Test A: Irradiance uniformity

Test A was an attempt to recreate the table in fig 2.6. The uniformity was measured at the exit port with different distances from the sphere while the white light source was at the center of the input port, fig 3.25. This test was made with the three spheres, tab 3.2.

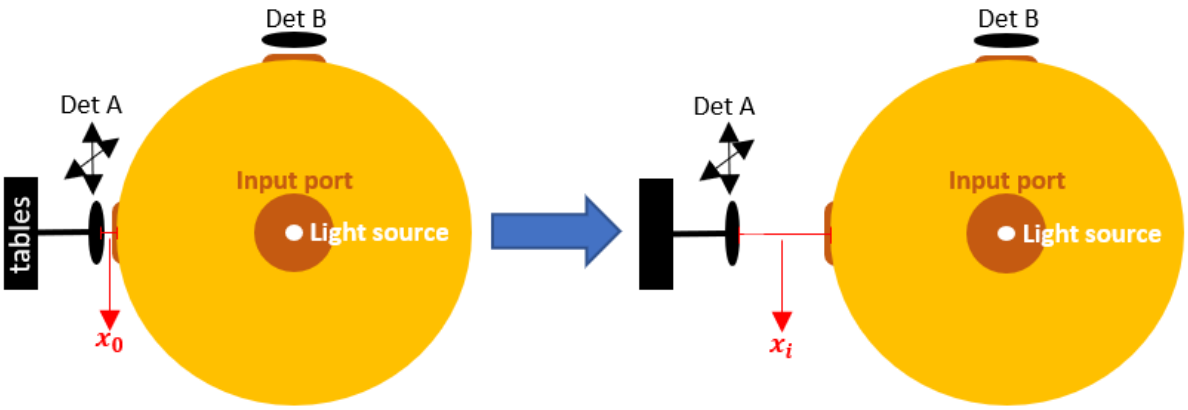

Figure 3.25: Schematization of test A: the uniformity was measured at the exit port with different distances x, while the white light source was at the center of input port.

	Big Sphere	**Small Sphere**	**Globe**
x **(±0,025mm)**	18,1	8,7	7,6
	23,0	11,7	129,3
	32,9	16,6	251,3
	38,1	21,8	-
	54,9	-	-
	77,1	-	-
	95,5	-	-
	113,3	-	-
	168,9	-	-
	249,1	-	-
	312,4	-	-

Table 3.2: Distances x from the exit port for each IS in test A. The values have been rounded to the first decimal.

Although it was not possible to cover all positions in fig 2.6 due to mechanical limitations, those distances above tried to cover it. Since the BS is bigger, it was decided that more points would be measured; the globe is similar to the BS but it is not a real sphere, so after the third distance there were a lot of discrepancies.

3.2.2 Test B: Irradiance uniformity with a monochromatic Blue and a Red light

In test B, the uniformity was measured at the exit port at the closest distance from the sphere while a fiber was at the center of the input port, tab 3.3. This test was repeated twice for blue, fig 3.26, and red light sources and was made with the three spheres.

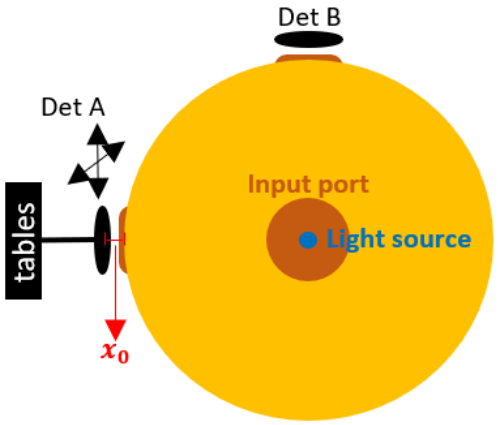

Figure 3.26: Schematization of test B: the uniformity was measured at the exit port at closest distance, while the blue light source was at the center of input port. It's reciprocal for the red light source.

	Big Sphere	Small Sphere	Globe
$x(\pm 0{,}025\text{mm})$	23,0	8,7	7,6

Table 3.3: Distances x from the exit port for each IS in test B. The values have been rounded to the first decimal.

3.2.3 Test C: Irradiance uniformity sensitivity with light injection angle

The test C was only made with the BS with white light. It was intended to discover how sensible the sphere was to the light injection with different angles, and it was only made with BS to study the sphericity factor.

The uniformity was measured at the exit port at the same distance $(23,0 \pm 0,025mm)$ while the light source had different positions at the input port, and with different positions with a $45°$ angle. It was measured on the left, right and up side of the port, fig 3.27, and was measure with an angle of $45°$, twice in the left and right side, and once in the up side of the input port, fig 3.28.

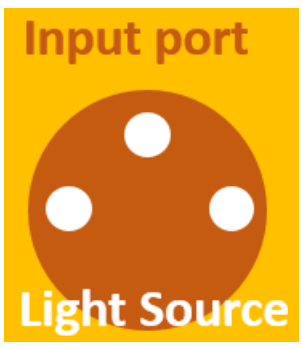

Figure 3.27: Schematization of test C: the little white circles are the different positions of the white light source at the input source.

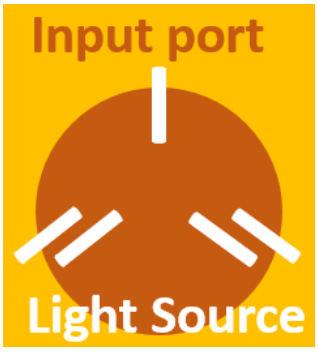

Figure 3.28: Schematization of test C: the white rectangles are the different angles of the white light source at the input source.

3.2.4 Test D: Irradiance uniformity sensitivity to injection f-number

Test D was only made with the SS with white light. It was intended to discover how sensible the sphere was to the light injection with different f-numbers. The uniformity was measured at the exit port at different distances, table 3.4, from the sphere while the light source passed through a lens and a diaphragm before reaching the IS. Hence, some calculations were necessary for the assembly.

To test that sensibility, an optical set up was implemented. Every optical system is characterized by an aperture stop, that determines the amount of light that passes through it. For a given aperture diameter, d, and focal length, f, we can calculate the optics F-number[20]:

$$f/\# = \frac{f}{d} \tag{3.1}$$

Since the lens was used had a $d = 55mm$ and a $f = 200mm$, the f-number of the lens was $f/\# = 3,6$.

The magnification, M, of an optics describes the ratio between the image, s', and the position relative to the lens, s, and has an absolute value[20]:

$$M = \frac{s'}{s} \tag{3.2}$$

The reason of magnification is already known because the image of the sun that is intended to calculate is $3,7mm$ and the object size, the light source, is $4,5mm$.

Knowing this, and it is important to note that s and s' are not the same in the following formula, we can use the Gaussian Lens formula to discover the distance of the image:

$$\frac{1}{s} + \frac{1}{s'} = \frac{1}{f} \Leftrightarrow \frac{1}{s} + \frac{1}{sM} = \frac{1}{f} \Leftrightarrow \frac{1}{s}(1 + \frac{1}{M}) = \frac{1}{f} \Leftrightarrow s = 443mm \Longleftrightarrow s' = 364mm \tag{3.3}$$

Knowing the diameter of the lens and the image size, it can be calculated the f-number minimum[20]:

$$f/\#_{min} = \frac{s'}{d} = \frac{364}{55} = 6,6 \approx 7 \tag{3.4}$$

The maximum diameter that the diaphragm can reach is $46mm$, so the focal distance can be calculated

$$f = 46 * 7 = 322mm \tag{3.5}$$

A plane mirror (with $50mm$ of length) was added to the configuration, since the source beam will be directed to the middle of the mirror with an angle of $45°$, in order to do that the focal distance needs to be calculated as well.

$$\frac{50}{\sqrt{2}} * 6 \approx 210mm \tag{3.6}$$

All of these measurements were to create the scheme in figure 3.29 and the representation in laboratory right beside it, figure 3.30.

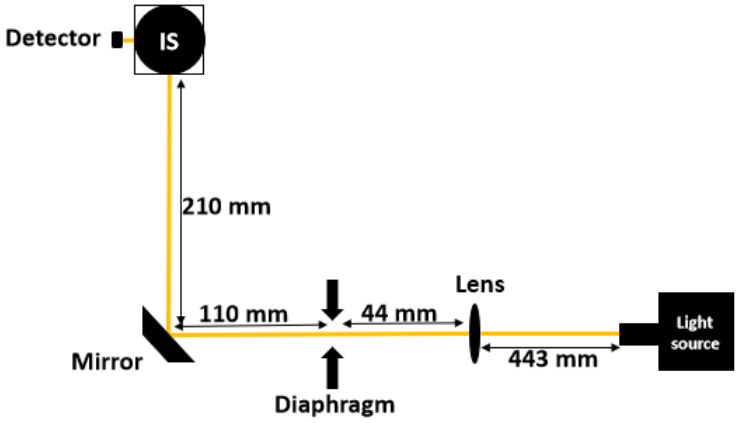

Figure 3.29: Schematization of the integrating sphere with imaging optics (mirror, diaphragm, lens and light source) at the previously calculated distances.

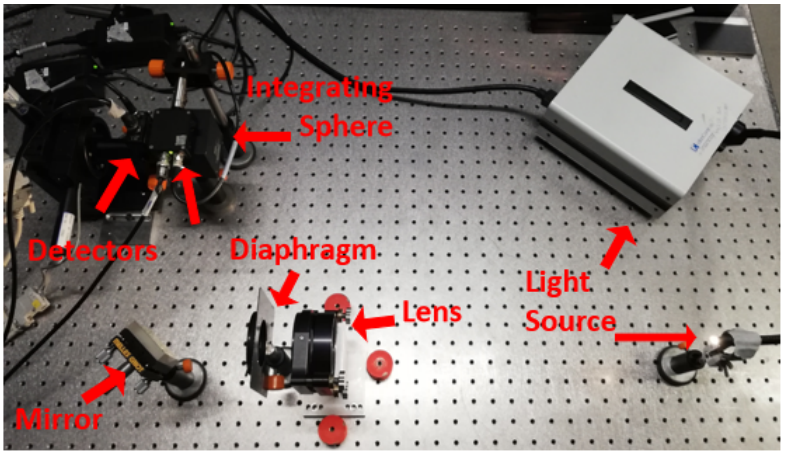

Figure 3.30: Photograph o the set-up of the fig 3.30 made in the laboratory and the identification of the imaging optics.

Since the minimum $f/\#$ that the diaphragm could give was $6,3$ and the maximum was 10, it was decided to measured the uniformity for five f-numbers but not with all the positions. With table 3.5, it is shown that the uniformity was measured in all positions at the minimum, middle and maximum f-number; while at intermediate f-numbers were only measured at the closest distance to the exit port.

	Small Sphere
x **(±0,0025cm)**	0,02
	0,36
	0,87
	1,36

Table 3.4: Distances x from the exit port in test D.

		x **(±0,025mm)**			
Diaphragm (mm)	**f/#**	**0,2**	**3,6**	**8,7**	**13,6**
49	6,3	✓	✓	✓	✓
44	7	✓	-	-	-
38,75	8	✓	✓	✓	✓
34,4	9	✓	-	-	-
31	10	✓	✓	✓	✓

Table 3.5: The distances from the exit port and f-numbers chosen to measure the uniformity in Test D.

3.2.5 Test E: Integrating sphere throughput

A powermeter was used for calibrated power measurements. This test was made with all the spheres and all the light sources.

It consists of using the powermeter (subsection 3.1.5) to measure the radiation: first at the light source, then at the exit port of detector B, then back to the light source and then at the exit port of detector A. And this process is repeated twelve times, a random number, to have a better repeatability, having 24 points for each port.

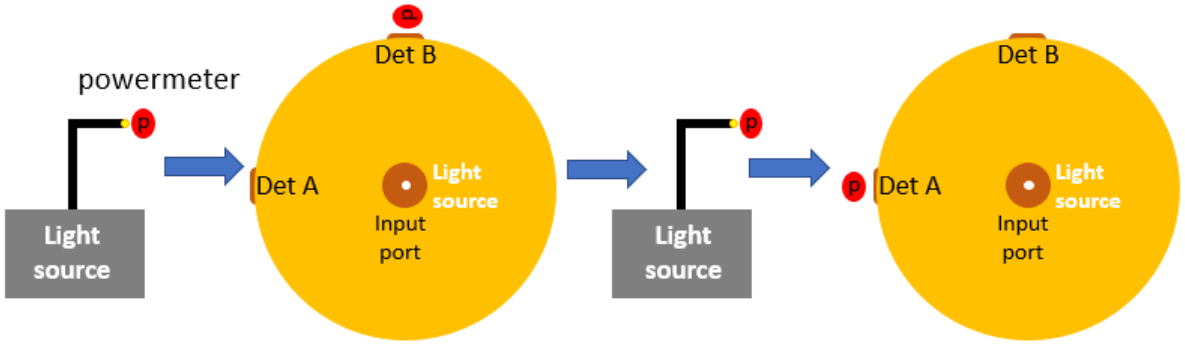

Figure 3.31: The radiation was measured at light source, then on the port of Det B, back to light and then on the port of Det A. This cycle was repeated.

The powermeter provides the maximum and minimum amplitude, and it has to wait for $\approx 5s$ in the position until the value stabilizes, due to the light source oscillations. It was measured in both ports only to have more points and to reassure that in every port, the output is the same.

It was considered the average value of the mean interval of oscillation before and the mean interval of oscillation after. This means that the variation in oscillations has as little impact as possible. This happens for the source as well as the port. And the sphere irradiance is calculated.

In this test, it was used two small spheres to compare with themselves. They are identical, the only thing that varies is that the new sphere is brand new, and it will be called the SS #2, while the SS #1 being the 'old one' that was used in the previous tests. So this will be a great comparison between new and old equipment.

3.2.6 Test F: Integrating sphere spectral response

A spectrometer was used to verify what the integrating sphere filters and the spectral response of the sphere was obtained.

In this test a spectrometer (subsection 3.1.6) was used to obtain the spectrum of the small sphere with white light source. The white light was at the center of the input port, the spectrometer was at the exit port, and the spectrometer measured close to the sphere and far from the sphere.

To recap, in the table 3.6 is a summary of all the tests.

Test	Name	Description	Spheres
A	Irradiance uniformity	Determine the irradiance uniformity of the spheres	BS, SS, Globe
B	Irradiance uniformity with a monochromatic Blue and Red light	Discover how sensible the sphere was to the light source	BS, SS, Globe
C	Irradiance uniformity sensitivity with light injection angle	Discover how sensible the sphere was to the position of light and to the angle of the light injection	BS
D	Irradiance uniformity sensitivity to injection f-number	Discover how sensible the sphere was to the light injection with different f-numbers	SS
E	Integrating sphere throughput	Used to calibrate power measurements	BS, SS#1 SS#2, Globe
F	Integrating sphere spectral response	Verify what the integrating sphere filters and the spectral response of the sphere was obtained	SS

Table 3.6: Summary of the tests with the respective name, description and spheres.

3.3 Interpolation of the theoretical uniformity

As said before, the experimental values will be compared to the table in fig 2.6. But before presenting the experimental results, is necessary to interpolated the theoretical uniformity values for each experimental test with the values from fig 2.6.

According to figure 2.5, the distance x will be the sum of the port width, the detector width and the distance from the port to the detector (l). And for each integrating sphere, it was made an uniformity interpolation.

3.3.1 Big integrating sphere

First, for each distance l_{BS} it was calculated the fraction x/D_{BS} respectively, table 3.7:

l_{BS}**(±0,0025)cm**	x_{BS}**(±0,025)mm**	x/D_{BS}
0,155	18,075	0,481
0,61	23,025	0,612
1,6	32,925	0,876
2,12	38,125	1,014
3,8	54,925	1,461
6,015	77,075	2,05
7,855	95,475	2,539
9,635	113,275	3,013
15,195	168,875	4,491
23,215	249,075	6,624
29,55	312,425	8,309

Table 3.7: x/D_{BS} values calculated for big integrating sphere

After calculating the fraction x/D_{BS}, it was interpolated the uniformity with the values in fig 2.6 for each experimental x/D_{BS}, and the result was, table 3.8:

d/D_{BS}—x/D_{BS}	**0,481**	**0,612**	**0,876**	**1,014**	**1,461**	**2,05**	**2,539**	**3,013**	**4,491**	**6,624**	**8,309**
0,1	1.00	1.00	1.00	1.00	1.00	1.00	1.00	1.00	1.00	1.00	1.00
0,2	0,98	0,98	0,99	0,99	0,99	1.00	1.00	1.00	1.00	1.00	1.00
0,3	0,96	0,96	0,97	0,97	0,98	0,99	0,99	1.00	1.00	1.00	1.00
0,4	0,92	0,92	0,94	0,95	0,97	0,98	0,99	0,99	0,99	1.00	1.00
0,5	0,88	0,89	0,91	0,92	0,96	0,97	0,98	0,99	0,99	1.00	1.00
0,6	0,82	0,84	0,88	0,89	0,94	0,96	0,97	0,98	0,99	0,99	0,99
0,7	0,76	0,78	0,84	0,86	0,92	0,95	0,96	0,97	0.98	0,99	0,99
0,8	0,70	0,73	0,79	0,82	0,88	0,93	0,95	0,97	0,98	0,99	0,99
0,9	0,62	0,66	0,75	0,78	0,86	0,92	0,94	0,96	0,97	0,99	0,99

Table 3.8: Interpolated uniformity with the values in fig 2.6 for each experimental x/D_{BS} calculated in table 3.7. The uniformity values were reduced to two decimals like in fig 2.6.

3.3.2 Small integrating sphere

For each distance l_{SS} it was calculated the fraction x/D_{SS} respectively, table 3.9:

l_{SS}**(±0,0025)cm**	x_{SS}**(±0,025)mm**	x/D_{SS}
0,055	8,675	0,231
0,36	11,725	0,312
0,85	16,625	0,442
1,365	21,775	0,579

Table 3.9: x/D_{SS} values calculated for small integrating sphere

After calculating the fraction x/D_{SS}, it was interpolated the uniformity with the values in fig 2.6 for each experimental x/D_{SS}, and the result was, table 3.10:

d/D_{SS}—x/D_{SS}	**0,683**	**0,923**	**1,309**	**1,715**
0,1	1.00	1.00	1.00	1.00
0,2	0,98	0,99	0,99	0,99
0,3	0,96	0,97	0,98	0,98
0,4	0,93	0,94	0,96	0,97
0,5	0,89	0,91	0,94	0,96
0,6	0,85	0,88	0,92	0,95
0,7	0,80	0,84	0,90	0,93
0,8	0,74	0,80	0,86	0,91
0,9	0,69	0,76	0,84	0,89

Table 3.10: Interpolated uniformity with the values in fig 2.6 for each experimental x/D_{SS} calculated in table 3.9. The uniformity values were reduced to two decimals like in fig 2.6.

3.3.3 Globe

For each distance l_G it was calculated the fraction x/D_G respectively, table 3.11:

l_G**(±0,0025)cm**	x_G**(±0,025)mm**	x/D_G
0,025	7,575	0,253
12,2	129,325	4,311
24,4	251,325	8,378

Table 3.11: x/D_G values calculated for the globe

After calculating the fraction x/D_G, it was interpolated the uniformity with the values in fig 2.6 for each experimental x/D_G, and the result was, table 3.12:

d/D_G—x/D_G	**0,25**	**4,31**	**8,38**
0,1	1.00	1.00	1.00
0,2	0,99	1,00	1,00
0,3	0,97	1,00	1,00
0,4	0,94	0,99	1,00
0,5	0,90	0,99	1,00
0,6	0,85	0,99	0,99
0,7	0,78	0,98	0,99
0,8	0,69	0,98	0,99
0,9	0,59	0,97	0,99

Table 3.12: Interpolated uniformity with the values in fig 2.6 for each experimental x/D_G calculated in table 3.11. The uniformity values were reduced to two decimals like in fig 2.6.

3.3.4 Small integrating sphere with f-number

For each distance l_{SSD} it was calculated the fraction x/D_{SSD} respectively, table 3.13:

l_{SSD} **(±0,0025)cm**	x_{SSD} **(±0,025)mm**	x/D_{SSD}
0,02	8,325	0,656
0,36	11,725	0,923
0,87	16,825	1,325
1,36	21,725	1,711

Table 3.13: x/D_{SSD} values calculated for the small integrating sphere with imaging optics

After calculating the fraction x/D_{SSD}, it was interpolated the uniformity with the values in fig 2.6 for each experimental x/D_{SSD}, and the result was, table 3.14:

d/D_{SSD} — x/D_{SSD}	**0,656**	**0,923**	**1,325**	**1,711**
0,1	1,00	1,00	1,00	1,00
0,2	0,98	0,99	0,99	0,99
0,3	0,96	0,97	0,98	0,98
0,4	0,93	0,94	0,96	0,97
0,5	0,89	0,91	0,95	0,96
0,6	0,85	0,88	0,92	0,95
0,7	0,79	0,84	0,90	0,93
0,8	0,74	0,80	0,87	0,91
0,9	0,68	0,76	0,84	0,89

Table 3.14: Interpolated uniformity with the values in fig 2.6 for each experimental x/D_{SSD} calculated in table 3.13. The uniformity values were reduced to two decimals like in fig 2.6.

Chapter 4

Experimental Results

In this chapter, the data was recollected through the LabVIEW program and saved in a excel file; in that file the data was analysed through a Mathcad program where the experimental uniformity was calculated. The results will be presented for every test in their respective section. But first, here's an example of that analysis.

4.1 Analyze

In figure 4.1, the experimental uniformity results for the big sphere, when $x/D_{BS} = 0,4$, is presented in the excel file.

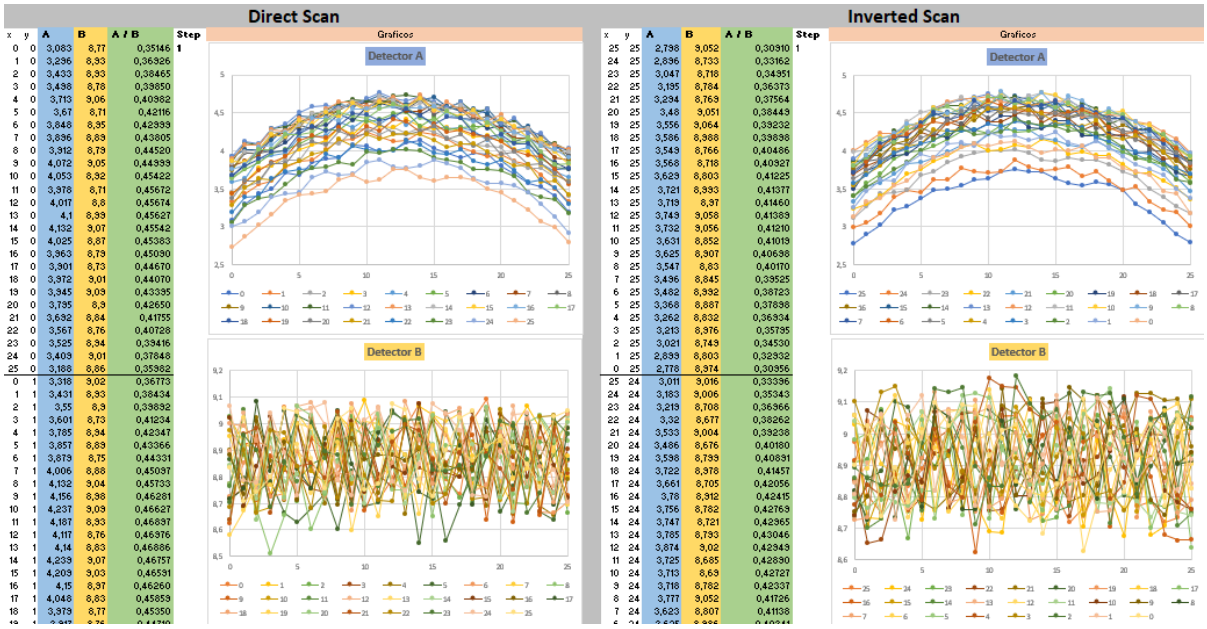

Figure 4.1: Experimental uniformity results for the big sphere, when $x/D_{BS} = 0,4$, presented in the excel file. The image is not complete.

The direct and inverted scans are shown in their respective, right and left side. For each scan, there are three arrays of values for each (x, y) position, and the step value. The detector A array and detector B are shown with the respective graph. (The arrays goes on until the positions are $(25, 25)$ but that's not relevant for the explanation.) The array A/B is the attenuation.

This information, fig 4.1, is analysed before the data goes to the Mathcad program, because the measure may need to be repeated. If the measure is approved it is carried into the program. The data that goes to the program are the positions x and y and the arrays A and B.

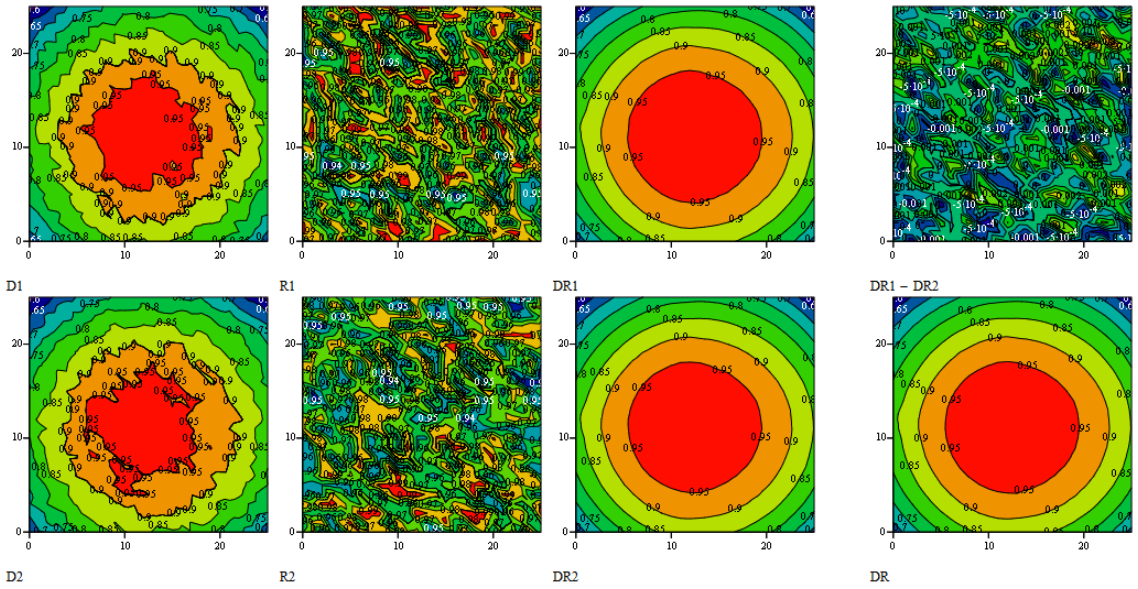

Figure 4.2: Contour plots for each scan.

In fig 4.2 the contour plots are presented: $D1$ contour plot is det A and $R1$ contour plot is det B, and $DR1$ contour plot is the fraction of A/B from the direct scan; and reciprocal for inverted. The $DR1 - DR2$ contour plot is the difference between direct and inverted scan. The DR is the average of the direct and inverted scan.

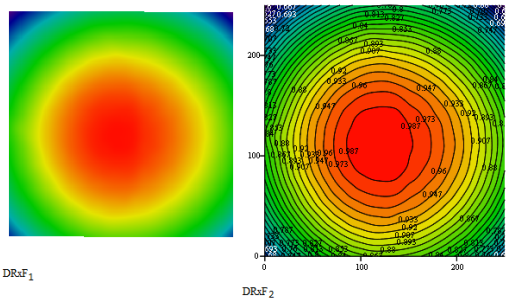

Figure 4.3: Contour plot DR multiplied by a factor, $DrxF_1$, e

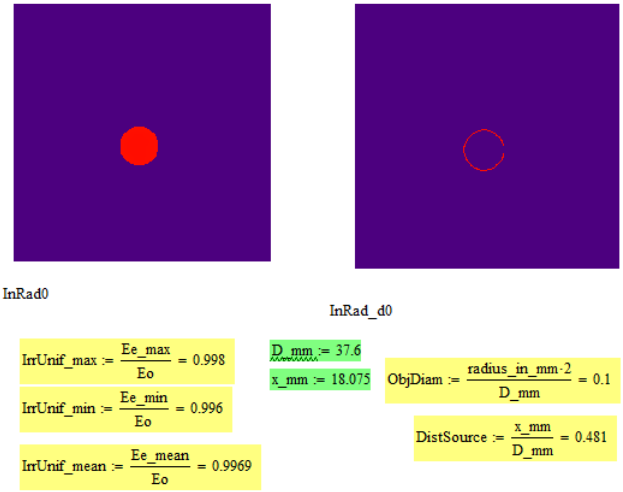

Figure 4.4: Uniformity calculated with $DRxF_2$ for $d/D_{BS} = 0,1$, when $x/D_{BS} = 0,4$.

In figure 4.3 shows $DrxF_1$ which is the real image, correspondent to DR, increased by a factor of 10 with interpolation; $DrxF_2$ is equal to $DrxF_1$ but with the various diameters around the centroid to help determine the uniformity. The centroid is where the center of sphere is.

In figure 4.4, $InRad0$ is the extraction of the complete circle of the uniformity E_e/E_o, from fig 2.5, when the fraction is $d/D_{BS} = 0,1$. The maximum, minimum and average E_e/E_o is

calculated. $InRad_d0$ is the perimeter of $d/D_{BS} = 0,1$.

Another two examples for the determination of the experimental uniformity, when $d/D_{BS} = 0,5$ and $d/D_{BS} = 0,9$, are figures 4.5 and 4.6.

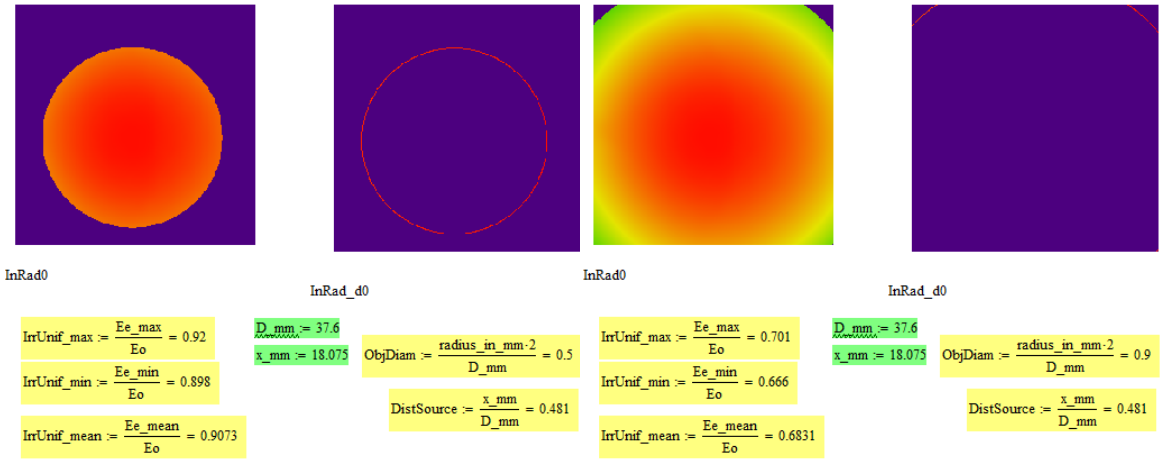

Figure 4.5: Uniformity calculated with $DRxF_2$ for $d/D_{BS} = 0,5$, when $x/D_{BS} = 0,4$.

Figure 4.6: Uniformity calculated with $DRxF_2$ for $d/D_{BS} = 0,9$, when $x/D_{BS} = 0,4$.

Big Sphere	x/D = 0,4			
d/D	EeMAX/Eo	EeMIN/Eo	EeMED/Eo	Variation
0,1	0,998	0,996	0,9969	0%
0,2	0,988	0,983	0,9856	1%
0,3	0,97	0,964	0,9675	1%
0,4	0,948	0,936	0,9414	3%
0,5	0,92	0,898	0,9073	5%
0,6	0,885	0,851	0,865	8%
0,7	0,839	0,797	0,8137	10%
0,8	0,777	0,732	0,7538	12%
0,9	0,701	0,666	0,6831	10%
	(Cx,Cy)	**12,205**	**11,189**	

Figure 4.7: Experimental uniformity results of the big sphere, when $x/D_{BS} = 0,4$.

Figure 4.7 is the final data collection. For every d/D_{BS}, has the respective maximum, minimum and average E_e/E_o. The centroid is also collected; this also show the detector is not exactly at the center of the port sphere, even though it was always reassured. The figure also presents the variation between average E_e/E_o and, maximum and minimum E_e/E_o, i.e. irradiance uniformity.

4.2 Test A: Irradiance uniformity

4.2.1 Big integrating sphere

Interpolated Results Big Sphere											
d/D|x/D	0.5	0.6	0.9	1.0	1.5	2.1	2.5	3.0	4.5	6.6	8.3
0.1	100%	100%	100%	100%	100%	100%	100%	100%	100%	100%	100%
0.2	98%	98%	99%	99%	99%	100%	100%	100%	100%	100%	100%
0.3	96%	96%	97%	97%	98%	99%	99%	100%	100%	100%	100%
0.4	92%	92%	94%	95%	97%	98%	99%	99%	100%	100%	100%
0.5	88%	89%	91%	92%	96%	97%	98%	99%	100%	100%	100%
0.6	82%	84%	88%	89%	94%	96%	97%	98%	99%	99%	100%
0.7	76%	78%	84%	86%	92%	95%	96%	97%	98%	99%	100%
0.8	70%	73%	79%	82%	88%	93%	95%	97%	98%	99%	100%
0.9	62%	66%	75%	78%	86%	92%	94%	96%	97%	99%	99%

Figure 4.8: Interpolated uniformity results of the big sphere in test A, for the different x/D_{BS}.

Experimental Results Big Sphere											
d/D|x/D	0.5	0.6	0.9	1.0	1.5	2.1	2.5	3.0	4.5	6.6	8.3
0.1	100%	99%	100%	100%	100%	100%	100%	100%	99%	99%	99%
0.2	99%	98%	98%	98%	99%	99%	99%	100%	99%	99%	98%
0.3	97%	96%	96%	96%	97%	98%	99%	99%	99%	99%	98%
0.4	94%	94%	92%	92%	94%	97%	98%	99%	99%	99%	98%
0.5	91%	90%	88%	88%	92%	95%	97%	98%	99%	98%	98%
0.6	87%	85%	82%	83%	88%	94%	96%	97%	98%	98%	98%
0.7	81%	79%	76%	77%	84%	91%	95%	96%	98%	98%	98%
0.8	75%	72%	70%	71%	80%	89%	93%	95%	98%	98%	98%
0.9	68%	64%	62%	65%	75%	86%	91%	94%	97%	98%	98%

Figure 4.9: Experimental uniformity results of the big sphere in test A, for the different x/D_{BS}.

(Exp - Inter) Results Big Sphere											
d/D|x/D	0.5	0.6	0.9	1.0	1.5	2.1	2.5	3.0	4.5	6.6	8.3
0.1	0%	-1%	0%	0%	0%	0%	0%	0%	-1%	-1%	-1%
0.2	0%	0%	0%	-1%	0%	-1%	-1%	-1%	-1%	-1%	-2%
0.3	1%	0%	-1%	-1%	-1%	-1%	0%	-1%	-1%	-1%	-2%
0.4	2%	1%	-2%	-3%	-2%	-1%	-1%	0%	-1%	-1%	-2%
0.5	3%	1%	-3%	-4%	-4%	-2%	-1%	-1%	-1%	-2%	-2%
0.6	4%	2%	-5%	-6%	-5%	-2%	-1%	-1%	0%	-1%	-2%
0.7	5%	1%	-7%	-9%	-7%	-4%	-1%	-1%	0%	-1%	-2%
0.8	5%	0%	-9%	-11%	-8%	-4%	-2%	-2%	-1%	-1%	-2%
0.9	7%	-2%	-12%	-14%	-11%	-6%	-3%	-2%	0%	-1%	-1%

Figure 4.10: The difference between the experimental and interpolated uniformity results of the big sphere in test A, for the different x/D_{BS}.

The table in fig 4.8 is the same as table 3.8, the difference is just the way is presented: with the colour gradient is visually better to compare with experimental uniformity results, fig 4.9. The table in fig 4.10 is the difference between the experimental and interpolated results.

4.2.2 Small integrating sphere

Interpolated Results Small Sphere				
d/D|x/D	0.7	0.9	1.3	1.7
0.1	100%	100%	100%	100%
0.2	98%	99%	99%	99%
0.3	96%	97%	98%	98%
0.4	93%	94%	96%	97%
0.5	89%	91%	94%	96%
0.6	85%	88%	92%	95%
0.7	80%	84%	90%	93%
0.8	74%	80%	86%	91%
0.9	69%	76%	84%	89%

Figure 4.11: Interpolated uniformity results of the small sphere in test A, for the different x/D_{SS}.

Experimental Results Small Sphere				
d/D|x/D	0.7	0.9	1.3	1.7
0.1	99%	100%	100%	100%
0.2	98%	98%	99%	99%
0.3	95%	95%	97%	98%
0.4	91%	91%	96%	97%
0.5	86%	87%	93%	96%
0.6	80%	82%	90%	94%
0.7	73%	77%	87%	92%
0.8	66%	71%	83%	90%
0.9	58%	65%	78%	88%

Figure 4.12: Experimental uniformity results of the small sphere in test A, for the different x/D_{SS}.

The table in fig 4.11 is the same as table 3.10; with the colour gradient is visually better to compare with experimental uniformity results, fig 4.12. The table in fig 4.13 is the difference between the experimental and interpolated results.

(Exp - Inter) Results Small Sphere				
d/D|x/D	0.7	0.9	1.3	1.7
0.1	-1%	0%	0%	0%
0.2	0%	-1%	0%	0%
0.3	-1%	-2%	0%	0%
0.4	-1%	-3%	-1%	0%
0.5	-3%	-5%	-1%	0%
0.6	-5%	-6%	-2%	-1%
0.7	-6%	-8%	-3%	-1%
0.8	-8%	-9%	-4%	-1%
0.9	-10%	-11%	-5%	-1%

Figure 4.13: The difference between the experimental and interpolated uniformity results of the small sphere in test A, for the different x/D_{SS}.

4.2.3 Globe

Interpolated Results Globe			
d/D|x/D	0.3	4.3	8.4
0.1	100%	100%	100%
0.2	99%	100%	100%
0.3	97%	100%	100%
0.4	94%	100%	100%
0.5	90%	100%	100%
0.6	85%	99%	100%
0.7	78%	98%	100%
0.8	69%	98%	100%
0.9	59%	97%	99%

Figure 4.14: Interpolated results of the globe in test A, for the different x/D_G.

Experimental Results Globe			
d/D|x/D	0.3	4.3	8.4
0.1	100%	98%	99%
0.2	100%	97%	99%
0.3	99%	98%	98%
0.4	99%	98%	98%
0.5	99%	97%	98%
0.6	99%	97%	98%
0.7	98%	97%	98%
0.8	98%	97%	99%
0.9	97%	97%	98%

Figure 4.15: Experimental results of the globe in test A, for the different x/D_G.

(Exp - Inter) Results Globe			
d/D|x/D	0.3	4.3	8.4
0.1	0%	-2%	-1%
0.2	1%	-3%	-1%
0.3	2%	-2%	-2%
0.4	5%	-2%	-2%
0.5	9%	-2%	-2%
0.6	14%	-1%	-1%
0.7	20%	-1%	-1%
0.8	29%	-2%	-1%
0.9	38%	-1%	-1%

Figure 4.16: The difference between the experimental and interpolated results of the globe in test A, for the different x/D_G.

The table in fig 4.14 is the same as table 3.12; with the colour gradient is visually better to compare with experimental uniformity results, fig 4.15. The table in fig 4.16 is the difference between the experimental and interpolated results.

4.2.4 Conclusions from test A

For the big sphere, the experimental results shows that for closer distances, when the object occupies 50% of the port, the model does not have good uniformity predictions. When $x/D_{BS} = 0,5$, the uniformity is better than expected, comparing with fig 4.8; after that, the uniformity decreases having a 14% of error only to improve to 1% with the increase of the distance to the source.

The big area in red in fig 4.10, gives credence to the model, specially if the object does not exceeds two thirds of the port, to ensure that the error is no greater than 10% of what the model predicts in terms of uniformity. A typical situation for the current application.

At first sight, comparing figures 4.11 and 4.12 from the small sphere with figures 4.8 and 4.9 from the BS, the values obtained are really similar to each other. But looking at fig 4.13, the

uniformity is better than in the BS, having an error of 11%. It was impossibly for the detector to be closer to the sphere and for bigger distances the uniformity would be closer to 100%, so these distances were good choices to observe the behaviour of the sphere.

In theory it is assumed that the coating is behaving in a Lambertian, i.e. perfect, way, but that doesn't mean that it still is. The sphere is insensitive, its variation is very small, so it is presumed to be doing its job. If the sphere were not Lambertian, the model might not be valid. Because closer to the sphere, there is an angular issue with respect to the light beams. While for farther distances, this problem is not critical, because the beam distributes more to larger angles, i.e. reflects more.

It only demonstrates that, even though the BS is older and bigger than SS, the degradation wasn't extreme and the size of the SS maintains the characteristics of uniformity.

For the globe at a closer distance is more homogeneous, and in terms of uniformity, the globe almost behaves like a sphere. The results were better than expected, and it was possible to measure distances closer to the sphere than with the others. And in this case, the influence whether the surface of the sphere is Lambertian or not is noticeable.

4.3 Test B: Irradiance Uniformity with a monochromatic Blue and a Red light

4.3.1 Big integrating sphere

Interpolated Results Big Sphere	
d/D|x/D	0.6
0.1	100%
0.2	98%
0.3	96%
0.4	92%
0.5	89%
0.6	84%
0.7	78%
0.8	73%
0.9	66%

Figure 4.17: Interpolated results of the big sphere in test B, when $x/D_{BS} = 0,6$.

Experimental Results Big Sphere			
	White	Blue	Red
d/D|x/D	0.6	0.6	0.6
0.1	100%	100%	100%
0.2	99%	99%	98%
0.3	96%	98%	97%
0.4	94%	96%	94%
0.5	90%	93%	91%
0.6	85%	90%	87%
0.7	80%	86%	83%
0.8	73%	82%	77%
0.9	65%	77%	70%

Figure 4.18: Experimental results of the big sphere in test B, when $x/D_{BS} = 0,6$.

(Exp - Inter) Results Big Sphere			
	White	Blue	Red
d/D|x/D	0.6	0.6	0.6
0.1	0%	0%	0%
0.2	1%	1%	0%
0.3	0%	2%	1%
0.4	1%	3%	2%
0.5	1%	4%	2%
0.6	2%	6%	4%
0.7	2%	8%	4%
0.8	0%	9%	4%
0.9	-1%	11%	4%

Figure 4.19: The difference between the experimental and interpolated uniformity results of the big sphere in test B, when $x/D_{BS} = 0,6$.

4.3.2 Small integrating sphere

Interpolated Results Small Sphere	
d/D|x/D	0.7
0.1	100%
0.2	98%
0.3	96%
0.4	93%
0.5	89%
0.6	85%
0.7	80%
0.8	74%
0.9	69%

Figure 4.20: Interpolated results of the small sphere in test B, when $x/D_{SS} = 0,7$.

Experimental Results Small Sphere			
	White	Blue	Red
d/D|x/D	0.7	0.7	0.7
0.1	99%	99%	100%
0.2	98%	98%	98%
0.3	95%	95%	96%
0.4	91%	91%	92%
0.5	86%	87%	88%
0.6	80%	81%	82%
0.7	73%	74%	76%
0.8	66%	70%	70%
0.9	58%	63%	63%

Figure 4.21: Experimental results of the small sphere in test B, when $x/D_{SS} = 0,7$.

(Exp - Inter) Results Small Sphere			
	White	Blue	Red
d/D|x/D	0.7	0.7	0.7
0.1	-1%	-1%	0%
0.2	0%	0%	0%
0.3	-1%	-1%	0%
0.4	-1%	-1%	0%
0.5	-3%	-3%	-2%
0.6	-5%	-3%	-3%
0.7	-6%	-6%	-3%
0.8	-8%	-5%	-5%
0.9	-10%	-5%	-5%

Figure 4.22: The difference between the experimental and interpolated uniformity results of the small sphere in test B, when $x/D_{SS} = 0,7$.

4.3.3 Globe

Interpolated Results Globe	
d/D|x/D	0.3
0.1	100%
0.2	99%
0.3	97%
0.4	94%
0.5	90%
0.6	85%
0.7	78%
0.8	69%
0.9	59%

Figure 4.23: Interpolated results of the Globe in test B, when $x/D_G = 0,3$.

Experimental Results Globe			
	White	Blue	Red
d/D|x/D	0.3	0.3	0.3
0.1	100%	100%	99%
0.2	100%	99%	99%
0.3	99%	99%	99%
0.4	99%	99%	99%
0.5	99%	99%	99%
0.6	99%	99%	99%
0.7	98%	99%	99%
0.8	98%	98%	99%
0.9	97%	98%	98%

Figure 4.24: Experimental results of the Globe in test B, when $x/D_G = 0,3$.

(Exp - Inter) Results Globe			
	White	Blue	Red
d/D|x/D	0.3	0.3	0.3
0.1	0%	0%	-1%
0.2	1%	0%	0%
0.3	2%	2%	2%
0.4	5%	5%	5%
0.5	9%	9%	9%
0.6	14%	14%	14%
0.7	20%	21%	21%
0.8	29%	29%	30%
0.9	38%	39%	39%

Figure 4.25: The difference between the experimental and interpolated uniformity results of the Globe in test B, when $x/D_G = 0,3$.

4.3.4 Conclusions from test B

When a monochromatic blue and a red light is injected in the big integrating sphere, it had much better results than with white light injected, fig 4.18. Comparing with the interpolated results, the uniformity varied 11% and 4% with blue an red light, respectively, fig 4.19.

With the small sphere, the results weren't so better than with big sphere, although the monochromatic Blue and a Red light had better results than the white light, fig 4.21. However,

the uniformity varied less than the big sphere, having a error of 5% for each light, fig 4.22.

From the spheres, the globe had the best experimental results, fig 4.24. But the uniformity had the worst error, with variation of 39%, fig 4.25. Since it must lose light and is not as efficient as the other spheres.

The conclusion is that, when the spectral part is concerned, it is necessary to have in account the size of the object. Since for the first one third, the variation was around 2% and deteriorated as the size increased. If using the full size of the output port, care must be taken with the spectral part, because the behaviour at the extremes is different in the visible, compared to the rest of the spectrum.

4.4 Test C: Irradiance Uniformity sensitivity with light injection angle

The interpolated results for this case is figure 4.17.

Experimental Results Big Sphere									
	Center	Left	Right	Up	Inc right 1	Inc left 1	Inc down	Inc right 2	Inc left 2
d/D|x/D	**0.6**	**0.6**	**0.6**	**0.6**	**0.6**	**0.6**	**0.6**	**0.6**	**0.6**
0.1	100%	100%	100%	100%	100%	99%	100%	100%	100%
0.2	99%	98%	98%	98%	98%	99%	98%	98%	98%
0.3	96%	96%	96%	96%	96%	97%	96%	96%	97%
0.4	94%	94%	94%	94%	94%	95%	94%	94%	94%
0.5	90%	90%	90%	90%	90%	91%	90%	90%	91%
0.6	85%	85%	85%	85%	85%	87%	86%	85%	86%
0.7	80%	80%	80%	80%	80%	81%	80%	80%	80%
0.8	73%	73%	73%	73%	72%	74%	73%	73%	73%
0.9	65%	66%	65%	65%	64%	66%	65%	65%	65%

Figure 4.26: Experimental uniformity results, with different injection angles,of the big sphere in test C, when $x/D_{BS} = 0,6$.

(Exp - Center Exp) Results Big Sphere								
	Left	Right	Up	Inc right 1	Inc left 1	Inc down	Inc right 2	Inc left 2
d/D|x/D	**0.6**	**0.6**	**0.6**	**0.6**	**0.6**	**0.6**	**0.6**	**0.6**
0.1	0%	0%	0%	0%	0%	0%	0%	0%
0.2	0%	0%	0%	0%	0%	0%	0%	0%
0.3	0%	0%	0%	0%	1%	0%	0%	0%
0.4	0%	0%	0%	0%	1%	0%	0%	0%
0.5	0%	0%	0%	0%	1%	0%	0%	1%
0.6	0%	0%	0%	0%	1%	0%	0%	1%
0.7	0%	0%	0%	0%	1%	0%	0%	0%
0.8	0%	0%	0%	0%	1%	0%	0%	0%
0.9	1%	0%	0%	-1%	1%	0%	0%	0%

Figure 4.27: The difference between the experimental (with different injection angles) and experimental center uniformity results of the big sphere in test C, when $x/D_{BS} = 0,6$.

(Exp - Inter) Results Big Sphere								
	Left	Right	Up	Inc right 1	Inc left 1	Inc down	Inc right 2	Inc left 2
d/D|x/D	0.6	0.6	0.6	0.6	0.6	0.6	0.6	0.6
0.1	0%	0%	0%	0%	-1%	0%	0%	0%
0.2	0%	0%	0%	0%	1%	0%	0%	0%
0.3	0%	0%	0%	0%	1%	0%	0%	1%
0.4	1%	1%	1%	1%	2%	1%	1%	2%
0.5	1%	1%	1%	1%	2%	1%	1%	2%
0.6	2%	2%	2%	1%	3%	2%	2%	2%
0.7	2%	1%	2%	1%	3%	2%	1%	2%
0.8	0%	0%	0%	0%	1%	0%	0%	1%
0.9	0%	-1%	-1%	-2%	0%	-1%	-1%	-1%

Figure 4.28: The difference between the experimental (with different injection angles) and interpolated uniformity results of the big sphere in test C, when $x/D_{BS} = 0,6$.

In this test the experimental results, fig 4.26, were compared to the experimental values when the light source was at the center of the input port, fig 4.27; and compared to the interpolated results, fig 4.28.

And the conclusion is straight forward, the sensitivity of the injection of light source does not depend of the angle. The error is less than 2%, something that is not relevant for this work.

4.5 Test D: Irradiance Uniformity sensitivity to injection f-number

Interpolated Results Small Sphere				
d/D|x/D	0.7	0.9	1.3	1.7
0.1	100%	100%	100%	100%
0.2	98%	99%	99%	99%
0.3	96%	97%	98%	98%
0.4	93%	94%	96%	97%
0.5	89%	91%	95%	96%
0.6	84%	88%	92%	95%
0.7	79%	84%	90%	93%
0.8	74%	80%	87%	91%
0.9	68%	76%	84%	89%

Figure 4.29: Interpolated uniformity results of the small sphere in test D, with different x/D_{SS}.

The table in fig 4.29 is the same as table 3.14; with the colour gradient is visually better to compare with experimental uniformity results, figures 4.30, B.1, B.3 and B.5. The tables in figures 4.31, B.2, B.4, and B.6 are the difference between the experimental and interpolated results.

The white light source has a $f/\# = 1,37$ and in this test the f-number was increased to test the integrating sphere's sensitivity.

Experimental Results Small Sphere					
f/#	6.3	7	8	9	10
d/D|x/D	0.7	0.7	0.7	0.7	0.7
0.1	100%	100%	100%	100%	100%
0.2	98%	99%	98%	99%	98%
0.3	96%	96%	96%	97%	96%
0.4	93%	93%	93%	93%	93%
0.5	88%	88%	88%	89%	88%
0.6	82%	82%	82%	83%	83%
0.7	75%	75%	76%	76%	76%
0.8	67%	68%	68%	69%	69%
0.9	60%	60%	60%	61%	61%

Figure 4.30: Experimental uniformity results of the small sphere in test D for all f-numbers, when $x/D_{SS} = 0,7$.

(Exp - Inter) Results Small Sphere					
f/#	6.3	7	8	9	10
d/D|x/D	0.7	0.7	0.7	0.7	0.7
0.1	0%	0%	0%	0%	0%
0.2	0%	1%	0%	1%	0%
0.3	0%	0%	0%	1%	0%
0.4	0%	0%	0%	1%	0%
0.5	-1%	-1%	-1%	-1%	-1%
0.6	-3%	-2%	-2%	-2%	-2%
0.7	-4%	-4%	-4%	-3%	-3%
0.8	-6%	-6%	-6%	-5%	-5%
0.9	-8%	-8%	-7%	-7%	-6%

Figure 4.31: The difference between the experimental and interpolated uniformity results of the small sphere in test D for all f-numbers, when $x/D_{SS} = 0,7$.

The results when $f/\# = 6,3$, $f/\# = 8$ and $f/\# = 10$ are in appendix B.1.

At $x/D_{SS} = 0,7$, comparing the experimental uniformity with the different $f/\#$ themselves, the values do not vary much; see fig 4.30. And comparing with the interpolated results when $x/D_{SS} = 0,7$, the uniformity only varies 1% to 2%, fig 4.31.

Comparing the figures B.2, B.4 and B.6, the same conclusion is reached. The uniformity only varies 1% or 2% from each $f/\#$ for every x/D_{SS}. This only indicates that the influence of the f-number on uniformity is at most 1%, which may be negligible.

4.6 Test E: Integrating sphere throughput

Full results from this test are in the appendix B.2.

4.6.1 Big integrating sphere

	Port A			
	White (mW)	E_S Exp (mW/cm^2)	E_S Theo (mW/cm^2)	Variation E_S (Exp/Theo)
average	41,380	0,267	0,794	**0,34**
std. Dev.	0,399	0,005	0,008	
	1,0%	2,0%	1,0%	

Figure 4.32: Big integrating sphere throughput for white light source in port A, in test E.

	Port B			
	White (mW)	E_S Exp (mW/cm^2)	E_S Theo (mW/cm^2)	Variation E_S (Exp/Theo)
average	41,380	0,271	0,794	**0,34**
std. Dev.	0,517	0,003	0,010	
	1,3%	1,3%	1,3%	

Figure 4.33: Big integrating sphere throughput for white light source in port B, in test E.

	Port A			
	Blue (mW)	E_S Exp (mW/cm^2)	E_S Theo (mW/cm^2)	Variation E_S (Exp/Theo)
average	2,603	0,013	0,050	**0,26**
std. Dev.	0,081	0,000	0,002	
	3,1%	2,1%	3,1%	

Figure 4.34: Big integrating sphere throughput for blue light source in port A, in test E.

	Port B			
	Blue (mW)	E_S Exp (mW/cm^2)	E_S Theo (mW/cm^2)	Variation E_S (Exp/Theo)
average	2,601	0,013	0,050	**0,26**
std. Dev.	0,078	0,000	0,002	
	3,0%	2,0%	3,0%	

Figure 4.35: Big integrating sphere throughput for blue light source in port B, in test E.

	Port A			
	Red (mW)	E_S Exp (mW/cm^2)	E_S Theo (mW/cm^2)	Variation E_S (Exp/Theo)
average	2,295	0,014	0,044	**0,32**
std. Dev.	0,030	0,000	0,001	
	1,3%	1,7%	1,3%	

Figure 4.36: Big integrating sphere throughput for red light source with port A, in test E.

	Port B			
	Red (mW)	E_S Exp (mW/cm^2)	E_S Theo (mW/cm^2)	Variation E_S (Exp/Theo)
average	2,295	0,014	0,044	**0,33**
std. Dev.	0,032	0,000	0,001	
	1,4%	0,9%	1,4%	

Figure 4.37: Big integrating sphere throughput for red light source in port B, in test E.

4.6.2 Small integrating sphere

SS#1: 'old' SS

	Port A			
	White (mW)	E_S Exp (mW/cm^2)	E_S Theo (mW/cm^2)	Variation E_S (Exp/Theo)
average	36,440	3,126	10,870	**0,29**
std. Dev.	0,632	0,075	0,188	
	1,7%	2,4%	1,7%	

Figure 4.38: Small integrating sphere #1 throughput for white light source in port A, in test E.

	Port B			
	White (mW)	E_S Exp (mW/cm^2)	E_S Theo (mW/cm^2)	Variation E_S (Exp/Theo)
average	36,455	3,197	10,874	**0,29**
std. Dev.	0,629	0,193	0,188	
	1,7%	6,0%	1,7%	

Figure 4.39: Small integrating sphere #1 throughput for white light source in port B, in test E.

	Port A			
	Blue (mW)	E_S Exp (mW/cm^2)	E_S Theo (mW/cm^2)	Variation E_S (Exp/Theo)
average	2,585	0,180	0,771	**0,23**
std. Dev.	0,071	0,014	0,021	
	2,8%	7,6%	2,8%	

Figure 4.40: Small integrating sphere #1 throughput for blue light source in port A, in test E.

	Port B			
	Blue (mW)	E_S Exp (mW/cm^2)	E_S Theo (mW/cm^2)	Variation E_S (Exp/Theo)
average	2,585	0,185	0,771	**0,24**
std. Dev.	0,086	0,021	0,026	
	3,3%	11,2%	3,3%	

Figure 4.41: Small integrating sphere #1 throughput for blue light source in port B, in test E.

	Port A			
	Red (mW)	E_S Exp (mW/cm^2)	E_S Theo (mW/cm^2)	Variation E_S (Exp/Theo)
average	2,255	0,164	0,673	**0,24**
std. Dev.	0,051	0,017	0,015	
	2,2%	10,6%	2,2%	

Figure 4.42: Small integrating sphere #1 throughput for red light source in port A, in test E.

	Port B			
	Red (mW)	E_S Exp (mW/cm^2)	E_S Theo (mW/cm^2)	Variation E_S (Exp/Theo)
average	2,256	0,173	0,673	**0,26**
std. Dev.	0,054	0,012	0,016	
	2,4%	7,0%	2,4%	

Figure 4.43: Small integrating sphere #1 throughput for red light source in port B, in test E.

SS#2: New SS

	Port A			
	White (mW)	E_S Exp (mW/cm^2)	E_S Theo (mW/cm^2)	Variation E_S (Exp/Theo)
average	102,047	7,726	30,439	**0,25**
std. Dev.	1,408	0,258	0,420	
	1,4%	3,3%	1,4%	

Figure 4.44: Small integrating sphere #2 throughput for white light source in port A, in test E.

	Port B			
	White (mW)	E_S Exp (mW/cm^2)	E_S Theo (mW/cm^2)	Variation E_S (Exp/Theo)
average	102,084	7,762	30,451	**0,25**
std. Dev.	1,436	0,297	0,428	
	1,4%	3,8%	1,4%	

Figure 4.45: Small integrating sphere #2 throughput for white light source in port B, in test E.

	Port A			
	Blue (mW)	E_S Exp (mW/cm^2)	E_S Theo (mW/cm^2)	Variation E_S (Exp/Theo)
average	2,603	0,013	0,050	**0,26**
std. Dev.	0,081	0,000	0,002	
	3,1%	2,1%	3,1%	

Figure 4.46: Small integrating sphere #2 throughput for blue light source in port A, in test E.

	Port B			
	Blue (mW)	E_S Exp (mW/cm^2)	E_S Theo (mW/cm^2)	Variation E_S (Exp/Theo)
average	2,601	0,013	0,050	**0,26**
std. Dev.	0,078	0,000	0,002	
	3,0%	2,0%	3,0%	

Figure 4.47: Small integrating sphere #2 throughput for blue light source in port B, in test E.

	Port A			
	Red (mW)	E_S Exp (mW/cm^2)	E_S Theo (mW/cm^2)	Variation E_S (Exp/Theo)
average	2,328	0,179	0,694	**0,26**
std. Dev.	0,040	0,003	0,012	
	1,7%	1,7%	1,7%	

Figure 4.48: Small integrating sphere #2 throughput for red light source in port A, in test E.

	Port B			
	Red (mW)	E_S Exp (mW/cm^2)	E_S Theo (mW/cm^2)	Variation E_S (Exp/Theo)
average	2,328	0,177	0,695	**0,25**
std. Dev.	0,041	0,007	0,012	
	1,8%	3,8%	1,8%	

Figure 4.49: Small integrating sphere #2 throughput for red light source in port B, in test E.

4.6.3 Globe

	Port A			
	White (mW)	E_S Exp (mW/cm^2)	E_S Theo (mW/cm^2)	Variation E_S (Exp/Theo)
average	182,195	0,268	0,778	**0,34**
std. Dev.	1,669	0,002	0,007	
	0,9%	0,9%	0,9%	

Figure 4.50: Globe throughput for white light source in port A, in test E.

	Port B			
	White (mW)	E_S Exp (mW/cm^2)	E_S Theo (mW/cm^2)	Variation E_S (Exp/Theo)
average	182,263	0,266	0,779	**0,34**
std. Dev.	1,718	0,004	0,007	
	0,9%	1,4%	0,9%	

Figure 4.51: Globe throughput for white light source in port B, in test E.

4.6.4 Conclusions from test E

In case of the BS, comparing the experimental and theoretical irradiance results from detector A and B: with white light there is no variation, figures 4.32 and 4.33; with blue light there is also no variation, figures 4.34 and 4.35; and with red light there is a variation of $0,01\%$, figures 4.36 and 4.37.

The experimental measurement corresponds to 33% of the theoretical model. This difference of variation is due to the model which is simple and optimistic and does not take into account the various aspects which make it reduce the throughput of the IS. It was tested what would be the reflectivity of the coating so that the variation was zero, and it gave 94%, which is a considerable reduction, which means that the sphere is quite degraded, however it must be due to the model that has to be adjusted.

For SS #1, comparing the experimental and theoretical irradiance results from detector A and B: with white light there is no variation, figures 4.38 and 4.39; with blue light there is a variation of $0,01\%$, figures 4.40 and 4.41; and with red light there is a variation of $0,02\%$, figures 4.42 and 4.43.

For SS #2, comparing the experimental and theoretical irradiance results from detector A and B: with white light there is no variation, figures 4.44 and 4.45; with blue light there is also no variation, figures 4.46 and 4.47; and with red light there is only a variation of $0,01\%$, figures 4.48 and 4.49.

Comparing the results from SS #1 with SS #2, the conclusion is that the degradation of the material is not as relevant as one might think, having a maximum error of $0,05\%$ between them. Assuming then that the coating has not changed, i.e. the reflectance is 99%, for a smaller spheres, the model the results give an excess of about 29%, for larger spheres it gives an excess of 33%, approximately. However, for this work is sufficient.

In the case of the globe, the sphere reflectance was compared with big sphere, with white light, and using the order of dimension from the variation between experimental and theoretical irradiance results, a reflectance of 90% was the best estimation. So for a classroom application, these results are more than sufficient, for uniformity it gave good results but for the irradiance they were not very good, but for the efficiency that it is, it works.

4.7 Test F: Integrating sphere spectral response

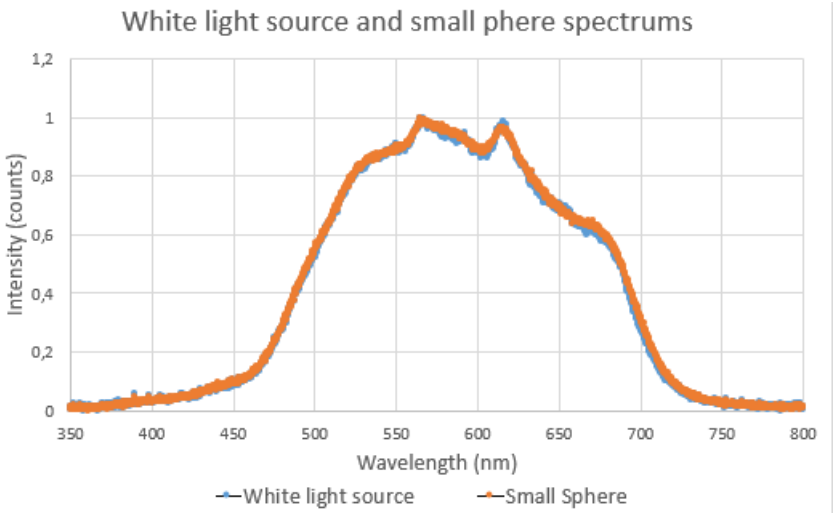

Figure 4.52: Small integrating sphere and white light source spectral response, in test F: in blue is the white light source and in orange is the small sphere.

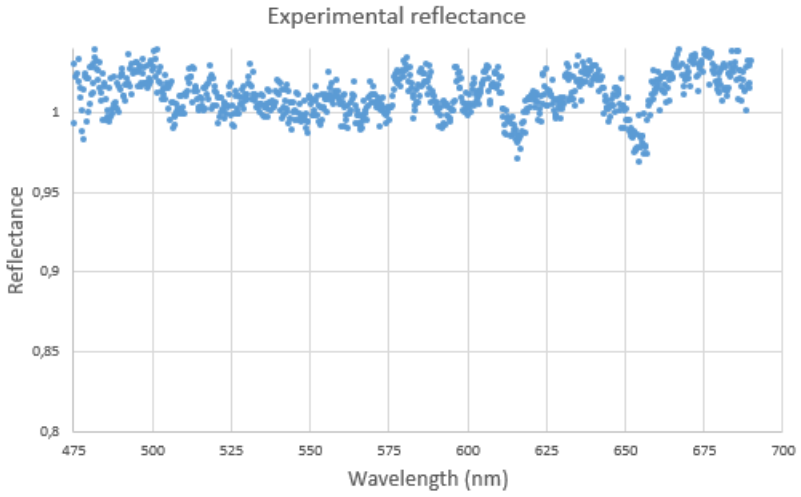

Figure 4.53: Experimental reflectance: small sphere spectrum divided by the white light spectrum, in test F.

The goal of this test was to confirm that the IS was not spectral filtering the light source, specially in the visible spectrum. The spectral response from the small sphere and white light source were obtained, fig 4.52. And the rate of the SS and white light is shown in fig 4.53, with this it can be compared with fig 3.5, and the sphere has a plane response in the visible spectrum, as expected. And outside of the visible spectrum, it is shown and influence as see in the previous test, but it is not relevant for the application.

Chapter 5

Conclusions

The goal of this thesis was to study integrating spheres, within the scope of astronomical instrumentation, to enable the integration of sunlight for further injection into a spectrograph, by means of an optical fibre. For that it was necessary to define a model that can describe the properties of and integrating sphere.

Several Monte Carlo Method models were studied. However, it was verified that they were complex and very time consuming, resulting in an accuracy that was not required for this application.

The search for a simplified model led it to the work developed by Labsphere[1], a known manufacturer of integrating spheres, where simplified versions of equations rule the behaviour of the light inside of the IS, presenting tables of irradiance, uniformity radiance and radiance response. That way, it was possible, in the scope of this thesis, to define a model and test it experimentally. The required accuracy for this application was 10% and this model was able to achieve that.

The experimental part was defined with different six tests to test the simplified model and the characterization of IS.

The test where the uniformity table in fig 2.6 was recreated, test A, the irradiance uniformity was measured at the exit of the exit port with different distances from the sphere while the white light source was at the center of the input port; this test was made for the three spheres. This test led to the following conclusions: the results of the BS and SS were a good comparison. Even though, it was possible to measure the uniformity for more distances with the BS, the results with SS overlap when the large sphere has its worst results; but comparing these two, the SS presents a better result. And although the BS is older, the variation between the two is not significant. The globe almost behaves like an IS, and the results were better than expected, and in this case it can be observed if the surface of the spheres is Lambertian or not.

In test B, the irradiance uniformity was measured at the exit port at the closest distance from the sphere while a fiber was at the center of the input port; this test was made for the three spheres and with blue and red light sources. And the results show that, when the spectral region is concerned, it is necessary to have in account the size of the object. Since for the first one third, the variation was around 2% and deteriorated as the size increased.

Test C consisted in testing the irradiance uniformity sensitivity with white light injection angle at the input port, and it was only made with big sphere. And in test D, it was tested the irradiance uniformity sensitivity with white light injection f-number at the input port, and it was only made with small sphere. With tests C and D, the results show that the irradiance

uniformity sensitivity does not depend of the injection angle and the injection f-number.

In test E, the integrating sphere throughput was determined for the three spheres and with each light source; and to determined the experimental irradiance. The conclusions are: with the BS, the experimental irradiance measured corresponds to 33% of the theoretical model. This difference of variation is due to the model which is simple and optimistic and does not take into account the various aspects which make it reduce the throughput of the IS, e.g. the coating reflectance. With the SS, assuming that the coating has not changed, the model the results give an excess of about 29%, for larger spheres it gives an excess of 33%, approximately. However, for this work is sufficient. The globe was compared to the BS, and the best estimation for the reflectance was 90%. So for classroom application, the results are sufficient.

And in test F, the spectrum of the small integrating sphere was calculated with white light. The results correspond to the expected values and it was confirmed that the small IS was not spectral filtering the light source, specially in the visible spectrum.

It is concluded that, the simplified model works and gives the pretended accuracy about an order of magnitude. There is 30% correction factor that must be applied to both large and small spheres when the reflectance is known. In terms of irradiance uniformity, the model for inferior object, about less than two thirds of the port, manages to characterize with a correction below 10%, which is what is necessary and more than enough.

The experimental part was very important, as it allowed to validate the model and characterize the sources, and experimentally verify and understand how the spheres varied with sources at the extreme end of the spectrum.

And with all of this information, it is possible to use this optical component within the system with the telescope, to integrate the sunlight into a fibre, that is connected to a spectrograph. And to understand what is the impact of the integrating sphere in the middle of the system.

A possible future work is to measure the reflectance uniformity of the sphere -to be able to validate more accurately the model in terms of radiance- and not to rely only on manufacture information; and to extend this work to smaller integrating spheres and more spheres with medium size, to compare the parameters with the variation of the sphere diameter.

Appendix A

Translation tables: block diagram in LabVIEW

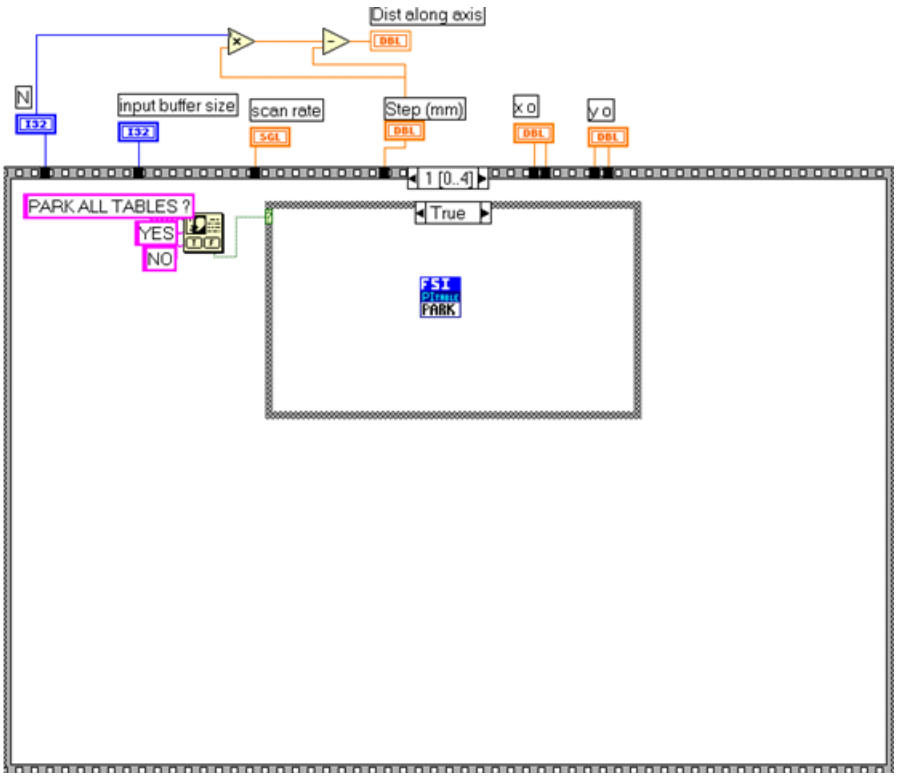

Figure A.1: Schematic of the graphical program that parks the tables.

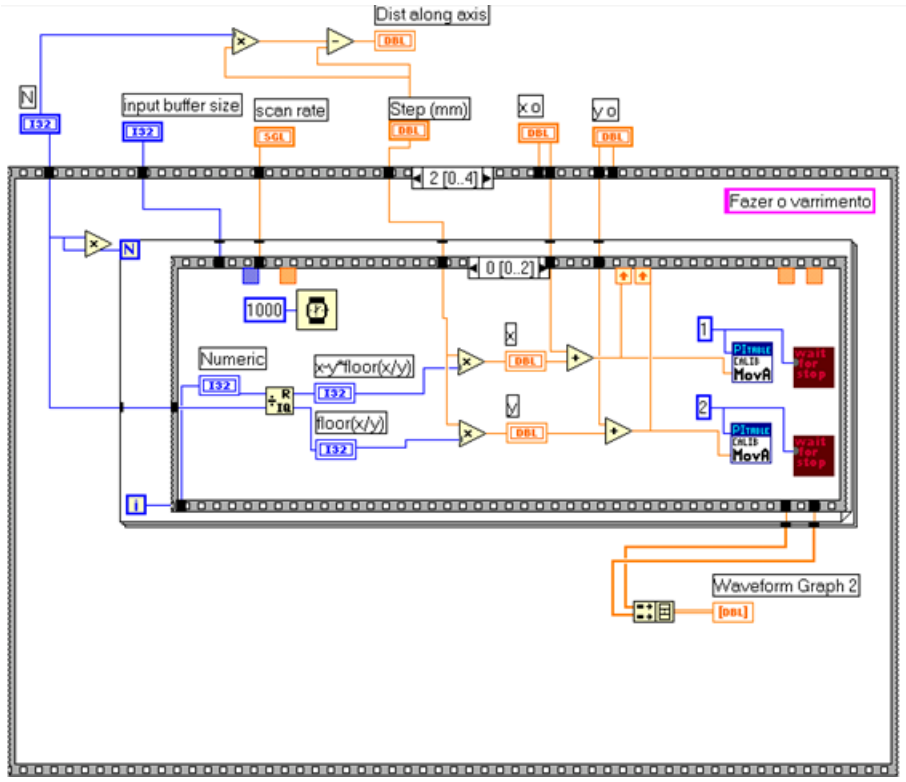

Figure A.2: Schematic of the graphical program that makes the direct movement as explained in 3.1.4 and shown in fig 3.20.

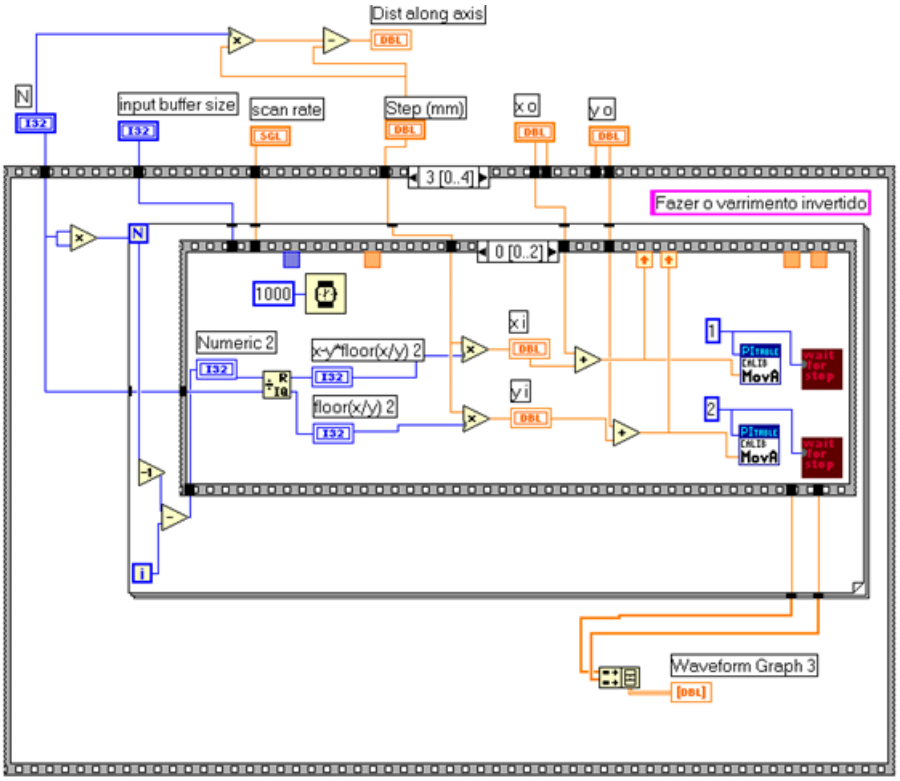

Figure A.3: Schematic of the graphical program that makes the inverted movement as explained in 3.1.4 and shown in fig 3.21.

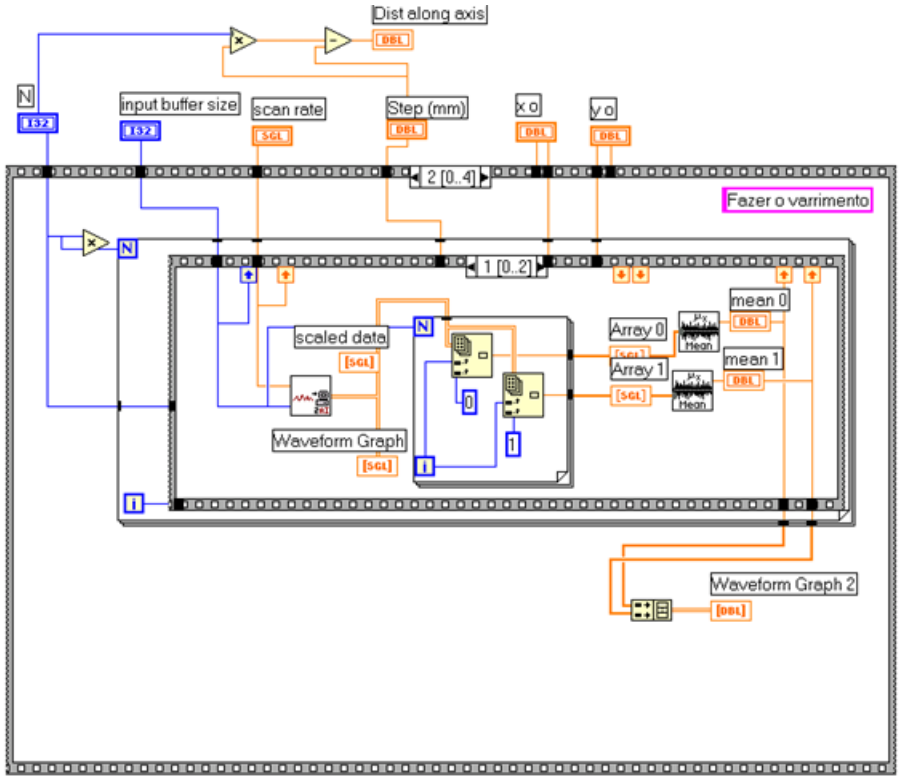

Figure A.4: Information is sent to the display for user purposes as explained in 3.1.4

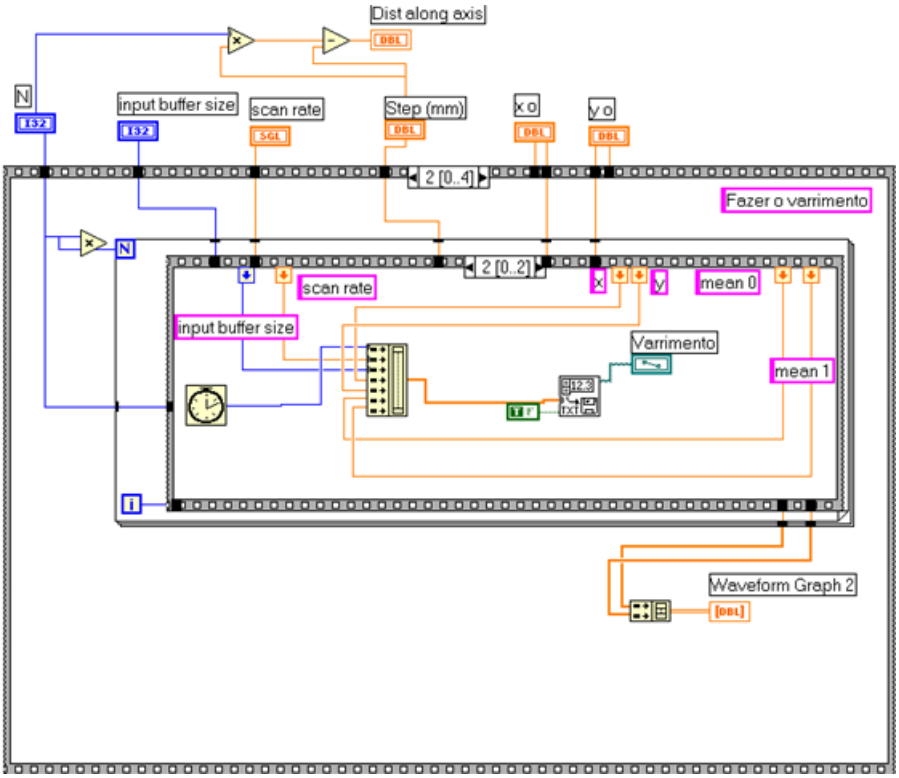

Figure A.5: Schematic of the graphical program that saves the chosen information in an excel file as explained in 3.1.4

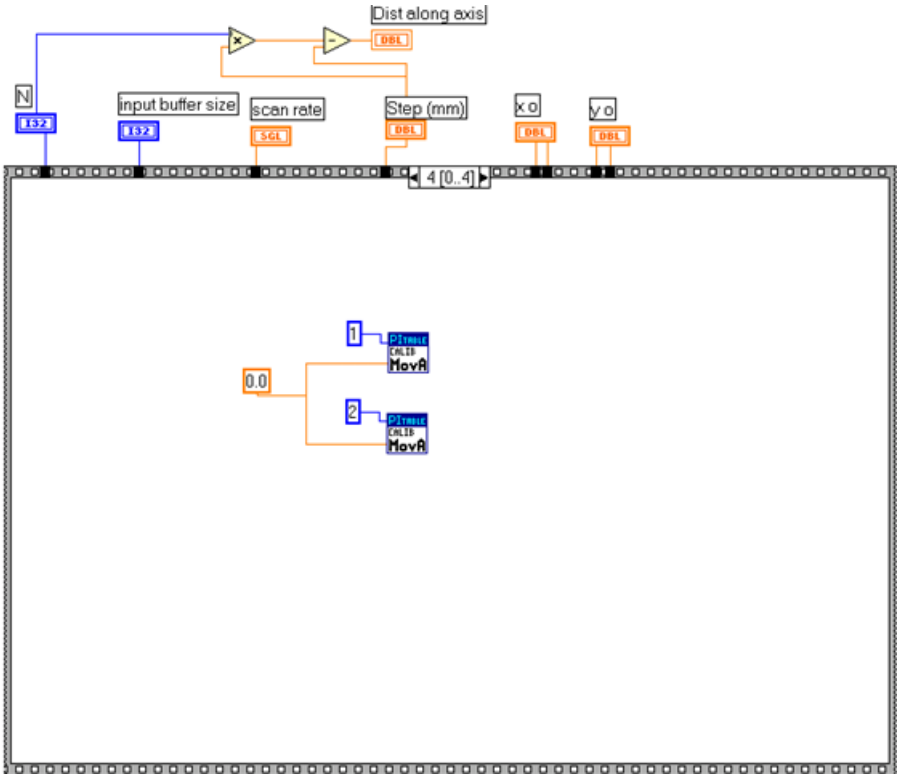

Figure A.6: Schematic of the graphical program that sends the table to the position $(0, 0)$ as explained in 3.1.4

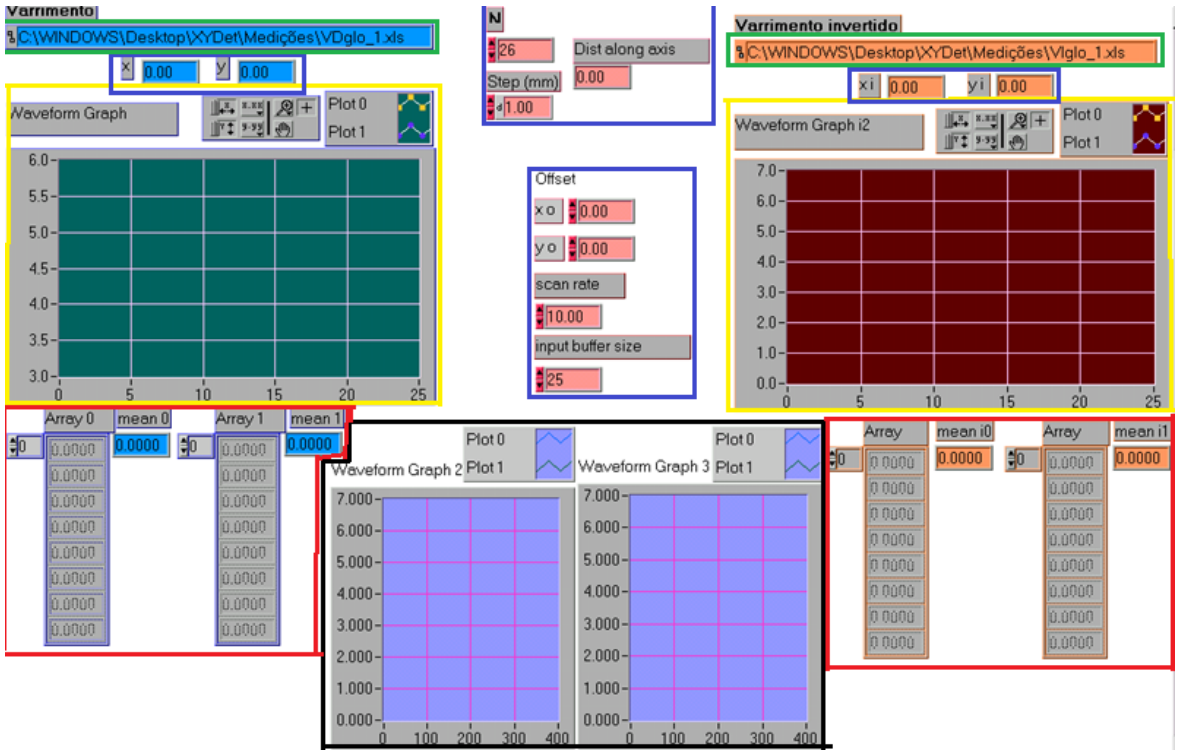

Figure A.7: Schematic of the graphical program of the user display as explained in 3.1.4

Appendix B

Results

B.1 Test D: Irradiance uniformity sensitivity to injection f-number

Experimental Results Small Sphere (f/#=6,3)				
d/D|x/D	0.7	0.9	1.3	1.7
0.1	100%	99%	100%	100%
0.2	98%	97%	99%	99%
0.3	96%	94%	97%	98%
0.4	93%	90%	95%	97%
0.5	88%	85%	92%	96%
0.6	82%	79%	88%	94%
0.7	75%	74%	84%	92%
0.8	67%	68%	80%	89%
0.9	60%	62%	75%	87%

Figure B.1: Experimental uniformity results of the small sphere in test D, when $f/\# = 6,3$.

(Exp - Inter) Results Small Sphere (f/#=6,3)				
d/D|x/D	0.7	0.9	1.3	1.7
0.1	0%	-1%	0%	0%
0.2	0%	-2%	0%	0%
0.3	0%	-3%	-1%	0%
0.4	0%	-5%	-2%	0%
0.5	-1%	-7%	-3%	0%
0.6	-3%	-9%	-4%	-1%
0.7	-4%	-11%	-6%	-1%
0.8	-6%	-13%	-7%	-1%
0.9	-8%	-14%	-9%	-3%

Figure B.2: The difference between the experimental and interpolated uniformity results of the small sphere in test D, when $f/\# = 6,3$.

Experimental Results Small Sphere (f/#=8)				
d/D|x/D	0.7	0.9	1.3	1.7
0.1	100%	99%	100%	100%
0.2	98%	97%	100%	99%
0.3	96%	94%	97%	98%
0.4	93%	90%	95%	97%
0.5	88%	85%	92%	96%
0.6	82%	80%	89%	94%
0.7	76%	74%	85%	92%
0.8	68%	68%	81%	90%
0.9	60%	62%	76%	87%

Figure B.3: Experimental uniformity results of the small sphere in test D, when $f/\# = 8$.

(Exp - Inter) Results Small Sphere (f/#=8)				
d/D|x/D	0.7	0.9	1.3	1.7
0.1	0%	-1%	0%	0%
0.2	0%	-2%	1%	-1%
0.3	0%	-3%	0%	0%
0.4	0%	-5%	-1%	0%
0.5	-1%	-6%	-3%	-1%
0.6	-2%	-8%	-4%	-1%
0.7	-4%	-10%	-5%	-1%
0.8	-6%	-12%	-6%	-1%
0.9	-7%	-13%	-8%	-2%

Figure B.4: The difference between the experimental and interpolated uniformity results of the small sphere in test D, when $f/\# = 8$.

Experimental Results Small Sphere (f/#=10)				
d/D|x/D	0.7	0.9	1.3	1.7
0.1	100%	99%	100%	100%
0.2	98%	97%	99%	99%
0.3	96%	94%	97%	98%
0.4	93%	90%	95%	98%
0.5	88%	86%	92%	96%
0.6	83%	80%	89%	95%
0.7	76%	75%	86%	93%
0.8	69%	69%	81%	91%
0.9	61%	64%	77%	88%

Figure B.5: Experimental uniformity results of the small sphere in test D, when $f/\# = 10$.

(Exp - Inter) Results Small Sphere (f/#=10)				
d/D|x/D	0.7	0.9	1.3	1.7
0.1	0%	-1%	0%	0%
0.2	0%	-1%	0%	0%
0.3	0%	-3%	-1%	0%
0.4	0%	-4%	-1%	0%
0.5	-1%	-6%	-2%	0%
0.6	-2%	-8%	-3%	0%
0.7	-3%	-9%	-4%	-1%
0.8	-5%	-11%	-5%	0%
0.9	-6%	-12%	-7%	-1%

Figure B.6: The difference between the experimental and interpolated uniformity results of the small sphere in test D, when $f/\# = 10$.

B.2 Test E: Integrating sphere throughput

B.2.1 Big integrating sphere

	Port A			
	White (mW)	E_S Exp (mW/cm^2)	E_S Theo (mW/cm^2)	Variation E_S (Exp/Theo)
1	40,203	0,260	0,772	0,34
2	41,623	0,265	0,799	0,33
3	41,323	0,271	0,793	0,34
4	41,770	0,272	0,802	0,34
5	41,575	0,264	0,798	0,33
6	41,698	0,259	0,800	0,32
7	41,133	0,269	0,789	0,34
8	41,148	0,264	0,790	0,33
9	41,980	0,265	0,806	0,33
10	41,723	0,264	0,801	0,33
11	41,508	0,261	0,797	0,33
12	41,660	0,257	0,799	0,32
13	41,475	0,265	0,796	0,33
14	41,900	0,267	0,804	0,33
15	41,815	0,261	0,802	0,33
16	41,193	0,275	0,791	0,35
17	41,058	0,266	0,788	0,34
18	41,475	0,259	0,796	0,33
19	41,063	0,270	0,788	0,34
20	41,065	0,275	0,788	0,35
21	41,180	0,275	0,790	0,35
22	41,108	0,268	0,789	0,34
23	41,580	0,270	0,798	0,34
24	40,872	0,272	0,784	0,35
average	41,380	0,267	0,794	**0,34**
std. Dev.	0,399	0,005	0,008	
	1,0%	2,0%	1,0%	

Figure B.7: Big integrating sphere throughput for white light source in port A, in test E.

	Port B			
	White (mW)	E_S Exp (mW/cm^2)	E_S Theo (mW/cm^2)	Variation E_S (Exp/Theo)
1	41,665	0,272	0,800	0,34
2	40,415	0,272	0,776	0,35
3	40,578	0,275	0,779	0,35
4	42,160	0,274	0,809	0,34
5	41,208	0,271	0,791	0,34
6	42,000	0,270	0,806	0,34
7	41,630	0,272	0,799	0,34
8	40,883	0,268	0,785	0,34
9	41,445	0,272	0,795	0,34
10	42,215	0,269	0,810	0,33
11	41,055	0,267	0,788	0,34
12	41,585	0,271	0,798	0,34
13	41,798	0,263	0,802	0,33
14	41,670	0,271	0,800	0,34
15	41,995	0,271	0,806	0,34
16	41,095	0,263	0,789	0,33
17	41,380	0,277	0,794	0,35
18	41,408	0,269	0,795	0,34
19	41,093	0,274	0,789	0,35
20	41,970	0,273	0,805	0,34
21	40,453	0,276	0,776	0,36
22	40,913	0,271	0,785	0,35
23	41,420	0,276	0,795	0,35
24	41,083	0,272	0,788	0,34
average	41,380	0,271	0,794	**0,34**
std. Dev.	0,517	0,003	0,010	
	1,3%	1,3%	1,3%	

Figure B.8: Big integrating sphere throughput for white light source in port B, in test E.

	Port A			
	Blue (mW)	E_S Exp (mW/cm^2)	E_S Theo (mW/cm^2)	Variation E_S (Exp/Theo)
1	2,389	0,013	0,046	0,28
2	2,445	0,013	0,047	0,28
3	2,604	0,013	0,050	0,25
4	2,645	0,012	0,051	0,25
5	2,482	0,013	0,048	0,28
6	2,540	0,013	0,049	0,26
7	2,655	0,013	0,051	0,25
8	2,658	0,012	0,051	0,24
9	2,628	0,013	0,050	0,25
10	2,637	0,013	0,051	0,26
11	2,682	0,013	0,051	0,26
12	2,686	0,013	0,052	0,25
13	2,636	0,013	0,051	0,25
14	2,551	0,013	0,049	0,27
15	2,673	0,013	0,051	0,26
16	2,543	0,013	0,049	0,26
17	2,621	0,013	0,050	0,25
18	2,653	0,012	0,051	0,24
19	2,666	0,013	0,051	0,25
20	2,496	0,013	0,048	0,27
21	2,672	0,013	0,051	0,25
22	2,661	0,013	0,051	0,25
23	2,620	0,013	0,050	0,26
24	2,622	0,013	0,050	0,26
average	2,603	0,013	0,050	**0,26**
std. Dev.	0,081	0,000	0,002	
	3,1%	2,1%	3,1%	

Figure B.9: Big integrating sphere throughput for blue light source in port A, in test E.

	Port B			
	Blue (mW)	E_S Exp (mW/cm^2)	E_S Theo (mW/cm^2)	Variation E_S (Exp/Theo)
1	2,463	0,012	0,047	0,26
2	2,507	0,013	0,048	0,26
3	2,402	0,013	0,046	0,27
4	2,622	0,012	0,050	0,25
5	2,649	0,013	0,051	0,25
6	2,434	0,013	0,047	0,28
7	2,607	0,013	0,050	0,25
8	2,652	0,013	0,051	0,25
9	2,651	0,013	0,051	0,26
10	2,630	0,013	0,050	0,26
11	2,670	0,013	0,051	0,25
12	2,669	0,013	0,051	0,25
13	2,656	0,013	0,051	0,25
14	2,620	0,013	0,050	0,25
15	2,592	0,013	0,050	0,25
16	2,646	0,012	0,051	0,25
17	2,585	0,013	0,050	0,25
18	2,575	0,013	0,049	0,26
19	2,688	0,013	0,052	0,25
20	2,542	0,012	0,049	0,26
21	2,607	0,013	0,050	0,26
22	2,687	0,013	0,052	0,26
23	2,612	0,013	0,050	0,26
24	2,653	0,012	0,051	0,25
average	2,601	0,013	0,050	**0,26**
std. Dev.	0,078	0,000	0,002	
	3,0%	2,0%	3,0%	

Figure B.10: Big integrating sphere throughput for blue light source in port B, in test E.

	Port A			
	Red (mW)	E_S Exp (mW/cm^2)	E_S Theo (mW/cm^2)	Variation E_S (Exp/Theo)
1	2,347	0,014	0,045	0,31
2	2,379	0,014	0,046	0,31
3	2,300	0,014	0,044	0,33
4	2,262	0,014	0,043	0,33
5	2,324	0,014	0,045	0,32
6	2,334	0,014	0,045	0,32
7	2,296	0,014	0,044	0,32
8	2,306	0,014	0,044	0,32
9	2,299	0,015	0,044	0,33
10	2,271	0,015	0,044	0,33
11	2,291	0,014	0,044	0,33
12	2,280	0,015	0,044	0,33
13	2,272	0,014	0,044	0,33
14	2,324	0,015	0,045	0,33
15	2,303	0,014	0,044	0,32
16	2,280	0,014	0,044	0,32
17	2,259	0,014	0,043	0,32
18	2,270	0,014	0,044	0,32
19	2,266	0,014	0,043	0,32
20	2,262	0,014	0,043	0,32
21	2,296	0,014	0,044	0,32
22	2,297	0,014	0,044	0,31
23	2,271	0,014	0,044	0,33
24	2,294	0,014	0,044	0,32
average	2,295	0,014	0,044	**0,32**
std. Dev.	0,030	0,000	0,001	
	1,3%	1,7%	1,3%	

Figure B.11: Big integrating sphere throughput for red light source in port A, in test E.

	Port B			
	Red (mW)	E_S Exp (mW/cm^2)	E_S Theo (mW/cm^2)	Variation E_S (Exp/Theo)
1	2,326	0,014	0,045	0,32
2	2,349	0,014	0,045	0,32
3	2,349	0,015	0,045	0,32
4	2,262	0,014	0,043	0,33
5	2,297	0,015	0,044	0,33
6	2,334	0,014	0,045	0,32
7	2,348	0,014	0,045	0,32
8	2,279	0,014	0,044	0,33
9	2,306	0,014	0,044	0,33
10	2,298	0,014	0,044	0,32
11	2,268	0,015	0,044	0,33
12	2,288	0,015	0,044	0,33
13	2,260	0,015	0,043	0,34
14	2,297	0,014	0,044	0,32
15	2,336	0,014	0,045	0,32
16	2,277	0,014	0,044	0,33
17	2,261	0,014	0,043	0,33
18	2,286	0,014	0,044	0,32
19	2,271	0,014	0,044	0,33
20	2,260	0,014	0,043	0,33
21	2,262	0,014	0,043	0,33
22	2,313	0,014	0,044	0,32
23	2,312	0,014	0,044	0,32
24	2,251	0,014	0,043	0,33
average	2,295	0,014	0,044	**0,33**
std. Dev.	0,032	0,000	0,001	
	1,4%	0,9%	1,4%	

Figure B.12: Big integrating sphere throughput for red light source in port B, in test E.

B.2.2 Small integrating sphere

	Port A			
	White (mW)	E_S Exp (mW/cm^2)	E_S Theo (mW/cm^2)	Variation E_S (Exp/Theo)
1	35,590	3,116	10,616	0,29
2	37,420	3,092	11,162	0,28
3	35,245	2,965	10,513	0,28
4	36,473	3,043	10,879	0,28
5	35,978	3,164	10,732	0,29
6	37,193	3,178	11,094	0,29
7	36,523	3,127	10,894	0,29
8	35,925	3,194	10,716	0,30
9	36,688	3,161	10,943	0,29
10	35,828	3,041	10,687	0,28
11	36,675	3,224	10,940	0,29
12	36,875	3,102	10,999	0,28
13	35,908	3,091	10,711	0,29
14	37,230	3,164	11,105	0,28
15	36,725	3,019	10,955	0,28
16	36,870	3,016	10,998	0,27
17	36,435	3,265	10,868	0,30
18	36,950	3,203	11,022	0,29
19	36,038	3,211	10,750	0,30
20	36,205	3,071	10,800	0,28
21	36,948	3,207	11,021	0,29
22	37,493	3,133	11,184	0,28
23	35,945	3,133	10,722	0,29
24	35,403	3,109	10,560	0,29
average	36,440	3,126	10,870	**0,29**
std. Dev.	0,632	0,075	0,188	
	1,7%	2,4%	1,7%	

Figure B.13: Small integrating sphere #1 throughput for white light source in port A, in test E.

	Port B			
	White (mW)	E_S Exp (mW/cm^2)	E_S Theo (mW/cm^2)	Variation E_S (Exp/Theo)
1	36,368	3,327	10,848	0,31
2	36,600	2,982	10,917	0,27
3	36,228	3,211	10,806	0,30
4	35,333	3,059	10,539	0,29
5	36,955	3,250	11,023	0,29
6	36,035	3,129	10,749	0,29
7	37,595	2,982	11,214	0,27
8	36,145	3,281	10,782	0,30
9	36,480	3,396	10,882	0,31
10	35,655	3,393	10,635	0,32
11	36,453	3,304	10,873	0,30
12	36,410	3,186	10,861	0,29
13	36,825	3,115	10,984	0,28
14	36,243	3,090	10,811	0,29
15	36,940	3,415	11,019	0,31
16	37,335	2,875	11,137	0,26
17	36,193	3,218	10,796	0,30
18	37,025	3,206	11,044	0,29
19	36,348	3,174	10,842	0,29
20	35,630	2,898	10,628	0,27
21	37,133	3,377	11,076	0,30
22	37,348	2,953	11,140	0,27
23	36,520	3,720	10,893	0,34
24	35,133	3,193	10,480	0,30
average	36,455	3,197	10,874	**0,29**
std. Dev.	0,629	0,193	0,188	
	1,7%	6,0%	1,7%	

Figure B.14: Small integrating sphere #1 throughput for white light source in port B, in test E.

	Port A			
	Blue (mW)	E_S Exp (mW/cm^2)	E_S Theo (mW/cm^2)	Variation E_S (Exp/Theo)
1	2,572	0,184	0,767	0,24
2	2,454	0,185	0,732	0,25
3	2,497	0,172	0,745	0,23
4	2,511	0,179	0,749	0,24
5	2,640	0,186	0,787	0,24
6	2,624	0,165	0,783	0,21
7	2,517	0,190	0,751	0,25
8	2,505	0,190	0,747	0,25
9	2,549	0,191	0,760	0,25
10	2,634	0,186	0,786	0,24
11	2,516	0,171	0,750	0,23
12	2,576	0,190	0,768	0,25
13	2,495	0,186	0,744	0,25
14	2,594	0,186	0,774	0,24
15	2,676	0,146	0,798	0,18
16	2,622	0,168	0,782	0,22
17	2,723	0,189	0,812	0,23
18	2,603	0,187	0,776	0,24
19	2,529	0,178	0,754	0,24
20	2,609	0,194	0,778	0,25
21	2,636	0,190	0,786	0,24
22	2,703	0,179	0,806	0,22
23	2,619	0,176	0,781	0,23
24	2,650	0,141	0,791	0,18
average	2,585	0,180	0,771	**0,23**
std. Dev.	0,071	0,014	0,021	
	2,8%	7,6%	2,8%	

Figure B.15: Small integrating sphere #1 throughput for blue light source in port A, in test E.

	Port B			
	Blue (mW)	E_S Exp (mW/cm^2)	E_S Theo (mW/cm^2)	Variation E_S (Exp/Theo)
1	2,571	0,198	0,767	0,26
2	2,501	0,187	0,746	0,25
3	2,431	0,108	0,725	0,15
4	2,518	0,180	0,751	0,24
5	2,647	0,191	0,789	0,24
6	2,643	0,174	0,788	0,22
7	2,562	0,187	0,764	0,24
8	2,366	0,198	0,706	0,28
9	2,646	0,175	0,789	0,22
10	2,504	0,173	0,747	0,23
11	2,565	0,174	0,765	0,23
12	2,662	0,205	0,794	0,26
13	2,521	0,202	0,752	0,27
14	2,581	0,194	0,770	0,25
15	2,598	0,191	0,775	0,25
16	2,644	0,189	0,789	0,24
17	2,660	0,163	0,793	0,21
18	2,725	0,192	0,813	0,24
19	2,498	0,195	0,745	0,26
20	2,598	0,174	0,775	0,22
21	2,643	0,204	0,788	0,26
22	2,630	0,167	0,785	0,21
23	2,639	0,205	0,787	0,26
24	2,702	0,203	0,806	0,25
average	2,585	0,185	0,771	**0,24**
std. Dev.	0,086	0,021	0,026	
	3,3%	11,2%	3,3%	

Figure B.16: Small integrating sphere #1 throughput for blue light source in port B, in test E.

	Port A			
	Red (mW)	E_S Exp (mW/cm^2)	E_S Theo (mW/cm^2)	Variation E_S (Exp/Theo)
1	2,142	0,163	0,639	0,25
2	2,287	0,095	0,682	0,14
3	2,233	0,175	0,666	0,26
4	2,207	0,175	0,658	0,27
5	2,296	0,153	0,685	0,22
6	2,336	0,150	0,697	0,22
7	2,231	0,174	0,665	0,26
8	2,239	0,175	0,668	0,26
9	2,271	0,172	0,677	0,25
10	2,329	0,166	0,695	0,24
11	2,354	0,173	0,702	0,25
12	2,331	0,173	0,695	0,25
13	2,254	0,171	0,672	0,25
14	2,187	0,166	0,652	0,25
15	2,242	0,147	0,669	0,22
16	2,248	0,174	0,671	0,26
17	2,263	0,175	0,675	0,26
18	2,288	0,163	0,682	0,24
19	2,238	0,143	0,668	0,21
20	2,246	0,161	0,670	0,24
21	2,220	0,170	0,662	0,26
22	2,197	0,174	0,655	0,27
23	2,224	0,170	0,663	0,26
24	2,257	0,173	0,673	0,26
average	2,255	0,164	0,673	**0,24**
std. Dev.	0,051	0,017	0,015	
	2,2%	10,6%	2,2%	

Figure B.17: Small integrating sphere #1 throughput for red light source in port A, in test E.

	Port B			
	Red (mW)	E_S Exp (mW/cm^2)	E_S Theo (mW/cm^2)	Variation E_S (Exp/Theo)
1	2,259	0,186	0,674	0,28
2	2,141	0,152	0,639	0,24
3	2,304	0,181	0,687	0,26
4	2,177	0,174	0,649	0,27
5	2,257	0,184	0,673	0,27
6	2,313	0,181	0,690	0,26
7	2,320	0,152	0,692	0,22
8	2,226	0,173	0,664	0,26
9	2,280	0,177	0,680	0,26
10	2,254	0,183	0,672	0,27
11	2,367	0,160	0,706	0,23
12	2,339	0,156	0,698	0,22
13	2,287	0,153	0,682	0,22
14	2,206	0,163	0,658	0,25
15	2,242	0,184	0,669	0,27
16	2,255	0,180	0,673	0,27
17	2,224	0,185	0,663	0,28
18	2,255	0,156	0,673	0,23
19	2,310	0,166	0,689	0,24
20	2,255	0,168	0,673	0,25
21	2,201	0,182	0,656	0,28
22	2,217	0,176	0,661	0,27
23	2,192	0,186	0,654	0,28
24	2,260	0,181	0,674	0,27
average	2,256	0,173	0,673	**0,26**
std. Dev.	0,054	0,012	0,016	
	2,4%	7,0%	2,4%	

Figure B.18: Small integrating sphere #1 throughput for red light source in port B, in test E.

	Port A			
	White (mW)	E_S Exp (mW/cm^2)	E_S Theo (mW/cm^2)	Variation E_S (Exp/Theo)
1	104,875	8,399	31,283	0,27
2	103,400	7,879	30,843	0,26
3	103,350	7,311	30,828	0,24
4	103,150	7,349	30,768	0,24
5	103,125	7,763	30,761	0,25
6	103,025	7,417	30,731	0,24
7	102,075	7,566	30,448	0,25
8	101,775	7,590	30,358	0,25
9	100,253	7,648	29,904	0,26
10	101,675	7,654	30,328	0,25
11	99,443	7,579	29,663	0,26
12	98,250	7,618	29,307	0,26
13	102,300	7,924	30,515	0,26
14	100,198	7,862	29,888	0,26
15	102,700	8,042	30,634	0,26
16	101,950	7,706	30,411	0,25
17	102,650	7,943	30,619	0,26
18	101,758	7,803	30,353	0,26
19	102,050	7,824	30,440	0,26
20	102,300	7,845	30,515	0,26
21	102,475	7,405	30,567	0,24
22	102,500	7,421	30,575	0,24
23	101,125	8,067	30,164	0,27
24	102,717	7,797	30,639	0,25
average	102,047	7,726	30,439	**0,25**
std. Dev.	1,408	0,258	0,420	
	1,4%	3,3%	1,4%	

Figure B.19: Small integrating sphere #2 throughput for white light source in port A, in test E.

	Port B			
	White (mW)	E_S Exp (mW/cm^2)	E_S Theo (mW/cm^2)	Variation E_S (Exp/Theo)
1	104,300	8,602	31,111	0,28
2	103,950	7,716	31,007	0,25
3	102,950	7,589	30,709	0,25
4	104,300	7,743	31,111	0,25
5	103,300	7,453	30,813	0,24
6	103,275	7,469	30,806	0,24
7	102,250	7,716	30,500	0,25
8	101,550	7,727	30,291	0,26
9	101,400	7,742	30,246	0,26
10	100,228	7,137	29,897	0,24
11	101,475	7,247	30,269	0,24
12	98,283	7,700	29,317	0,26
13	100,460	7,640	29,966	0,25
14	99,623	7,734	29,716	0,26
15	103,200	7,924	30,783	0,26
16	102,300	7,833	30,515	0,26
17	101,950	8,024	30,411	0,26
18	101,883	7,931	30,390	0,26
19	102,500	7,865	30,575	0,26
20	102,275	7,630	30,507	0,25
21	101,700	8,136	30,336	0,27
22	103,025	7,925	30,731	0,26
23	102,100	7,724	30,455	0,25
24	101,750	8,092	30,351	0,27
average	102,084	7,762	30,451	**0,25**
std. Dev.	1,436	0,297	0,428	
	1,4%	3,8%	1,4%	

Figure B.20: Small integrating sphere #2 throughput for white light source in port B, in test E.

Port A				
	Blue (mW)	E_S Exp (mW/cm^2)	E_S Theo (mW/cm^2)	Variation E_S (Exp/Theo)
1	2,683	0,169	0,800	0,21
2	2,757	0,194	0,822	0,24
3	2,671	0,190	0,797	0,24
4	2,731	0,202	0,814	0,25
5	2,706	0,192	0,807	0,24
6	2,767	0,194	0,825	0,23
7	2,399	0,191	0,716	0,27
8	2,753	0,201	0,821	0,24
9	2,765	0,191	0,825	0,23
10	2,698	0,201	0,805	0,25
11	2,723	0,202	0,812	0,25
12	2,638	0,195	0,787	0,25
13	2,671	0,202	0,797	0,25
14	2,669	0,199	0,796	0,25
15	2,623	0,191	0,782	0,24
16	2,535	0,175	0,756	0,23
17	2,622	0,198	0,782	0,25
18	2,688	0,201	0,802	0,25
19	2,691	0,207	0,803	0,26
20	2,682	0,209	0,800	0,26
21	2,582	0,206	0,770	0,27
22	2,684	0,204	0,801	0,26
23	2,689	0,198	0,802	0,25
24	2,638	0,205	0,787	0,26
average	2,669	0,197	0,796	**0,25**
std. Dev.	0,080	0,009	0,024	
	3,0%	4,8%	3,0%	

Figure B.21: Small integrating sphere #2 throughput for blue light source in port A, in test E.

Port B				
	Blue (mW)	E_S Exp (mW/cm^2)	E_S Theo (mW/cm^2)	Variation E_S (Exp/Theo)
1	2,699	0,180	0,805	0,22
2	2,684	0,198	0,801	0,25
3	2,699	0,170	0,805	0,21
4	2,692	0,182	0,803	0,23
5	2,722	0,196	0,812	0,24
6	2,754	0,195	0,821	0,24
7	2,555	0,198	0,762	0,26
8	2,582	0,201	0,770	0,26
9	2,761	0,187	0,823	0,23
10	2,726	0,199	0,813	0,24
11	2,709	0,198	0,808	0,25
12	2,673	0,184	0,797	0,23
13	2,669	0,203	0,796	0,25
14	2,688	0,206	0,802	0,26
15	2,698	0,205	0,805	0,25
16	2,515	0,198	0,750	0,26
17	2,642	0,207	0,788	0,26
18	2,631	0,206	0,785	0,26
19	2,678	0,201	0,799	0,25
20	2,632	0,201	0,785	0,26
21	2,661	0,200	0,794	0,25
22	2,627	0,204	0,784	0,26
23	2,661	0,203	0,794	0,26
24	2,679	0,202	0,799	0,25
average	2,668	0,197	0,796	**0,25**
std. Dev.	0,058	0,009	0,017	
	2,2%	4,8%	2,2%	

Figure B.22: Small integrating sphere #2 throughput for blue light source in port B, in test E.

Port A				
	Red (mW)	E_S Exp (mW/cm^2)	E_S Theo (mW/cm^2)	Variation E_S (Exp/Theo)
1	2,304	0,176	0,687	0,26
2	2,259	0,181	0,674	0,27
3	2,297	0,182	0,685	0,27
4	2,381	0,173	0,710	0,24
5	2,281	0,177	0,680	0,26
6	2,307	0,176	0,688	0,26
7	2,286	0,178	0,682	0,26
8	2,248	0,178	0,670	0,27
9	2,342	0,174	0,699	0,25
10	2,391	0,182	0,713	0,26
11	2,353	0,181	0,702	0,26
12	2,355	0,181	0,702	0,26
13	2,378	0,180	0,709	0,25
14	2,292	0,181	0,684	0,26
15	2,357	0,177	0,703	0,25
16	2,351	0,175	0,701	0,25
17	2,309	0,177	0,689	0,26
18	2,308	0,181	0,688	0,26
19	2,311	0,177	0,689	0,26
20	2,388	0,184	0,712	0,26
21	2,339	0,183	0,698	0,26
22	2,369	0,182	0,707	0,26
23	2,334	0,178	0,696	0,26
24	2,330	0,179	0,695	0,26
average	2,328	0,179	0,694	**0,26**
std. Dev.	0,040	0,003	0,012	
	1,7%	1,7%	1,7%	

Figure B.23: Small integrating sphere #2 throughput for red light source in port A, in test E.

Port B				
	Red (mW)	E_S Exp (mW/cm^2)	E_S Theo (mW/cm^2)	Variation E_S (Exp/Theo)
1	2,264	0,151	0,675	0,22
2	2,330	0,176	0,695	0,25
3	2,308	0,181	0,688	0,26
4	2,282	0,183	0,681	0,27
5	2,391	0,169	0,713	0,24
6	2,302	0,182	0,687	0,27
7	2,265	0,176	0,675	0,26
8	2,250	0,176	0,671	0,26
9	2,333	0,181	0,696	0,26
10	2,360	0,185	0,704	0,26
11	2,372	0,175	0,707	0,25
12	2,346	0,173	0,700	0,25
13	2,367	0,170	0,706	0,24
14	2,374	0,180	0,708	0,25
15	2,327	0,181	0,694	0,26
16	2,331	0,182	0,695	0,26
17	2,314	0,178	0,690	0,26
18	2,294	0,182	0,684	0,27
19	2,283	0,176	0,681	0,26
20	2,405	0,179	0,717	0,25
21	2,343	0,178	0,699	0,26
22	2,351	0,180	0,701	0,26
23	2,339	0,179	0,698	0,26
24	2,357	0,175	0,703	0,25
average	2,328	0,177	0,695	**0,25**
std. Dev.	0,041	0,007	0,012	
	1,8%	3,8%	1,8%	

Figure B.24: Small integrating sphere #2 throughput for red light source in port B, in test E.

B.2.3 Globe

	Port A			
	White (mW)	E_S Exp (mW/cm^2)	E_S Theo (mW/cm^2)	Variation E_S (Exp/Theo)
1	181,900	0,268	0,777	0,34
2	182,375	0,267	0,779	0,34
3	183,325	0,271	0,783	0,35
4	183,025	0,269	0,782	0,34
5	182,225	0,268	0,779	0,34
6	181,550	0,268	0,776	0,35
7	182,925	0,268	0,782	0,34
8	183,325	0,269	0,783	0,34
9	185,075	0,268	0,791	0,34
10	183,350	0,263	0,783	0,34
11	183,650	0,263	0,785	0,34
12	182,425	0,268	0,779	0,34
13	182,500	0,268	0,780	0,34
14	181,000	0,269	0,773	0,35
15	179,150	0,268	0,765	0,35
16	183,900	0,269	0,786	0,34
17	180,375	0,271	0,771	0,35
18	182,275	0,267	0,779	0,34
19	181,300	0,268	0,775	0,35
20	183,975	0,268	0,786	0,34
21	183,475	0,271	0,784	0,35
22	178,025	0,268	0,761	0,35
23	179,375	0,274	0,766	0,36
24	182,181	0,267	0,778	0,34
average	182,195	0,268	0,778	**0,34**
std. Dev.	1,669	0,002	0,007	
	0,9%	0,9%	0,9%	

Figure B.25: Globe throughput for white light source in port A, in test E.

	Port B			
	White (mW)	E_S Exp (mW/cm^2)	E_S Theo (mW/cm^2)	Variation E_S (Exp/Theo)
1	183,475	0,270	0,784	0,34
2	181,775	0,266	0,777	0,34
3	183,050	0,272	0,782	0,35
4	184,775	0,265	0,789	0,34
5	182,175	0,269	0,778	0,35
6	179,275	0,262	0,766	0,34
7	183,025	0,266	0,782	0,34
8	184,375	0,270	0,788	0,34
9	183,075	0,266	0,782	0,34
10	185,800	0,266	0,794	0,34
11	183,650	0,264	0,785	0,34
12	182,050	0,264	0,778	0,34
13	182,000	0,264	0,778	0,34
14	182,550	0,267	0,780	0,34
15	180,075	0,271	0,769	0,35
16	180,450	0,263	0,771	0,34
17	182,350	0,272	0,779	0,35
18	181,550	0,259	0,776	0,33
19	182,400	0,265	0,779	0,34
20	181,275	0,261	0,775	0,34
21	184,525	0,271	0,788	0,34
22	181,450	0,270	0,775	0,35
23	179,175	0,266	0,766	0,35
24	180,000	0,260	0,769	0,34
average	182,263	0,266	0,779	**0,34**
std. Dev.	1,718	0,004	0,007	
	0,9%	1,4%	0,9%	

Figure B.26: Globe throughput for white light source in port B, in test E.

Bibliography

[1] I. Labsphere, "Integrating sphere theory and applications," 2017.

[2] B. G. Crowther, "The design, construction, and calibration of a spectral diffuse/global irradiance meter," Master's thesis, The University of Arizona, 1997.

[3] S. N. M. Alexander V. Prokhorov and L. M. Hanssen, "Monte carlo modeling of an integrating sphere reflectometer," *Optical Society of America*, 2003.

[4] N. Corporation, "Spectralon diverging beam integrating spheres," 2020.

[5] O. D. Gröbel, "Integrating spheres: Product information," 2015.

[6] M. A. Inês Leite, Alexandre Cabral and N. Santos, "Imaging sensors for poet: a spatially resolved solar spectroscopy instrument." to be published in AOP2022 conference proceedings.

[7] ESO, "Harps: High accuracy radial velocity planet searcher."

[8] F. Pepe and et al., "Espresso at vlt. on-sky performance and first results," *Astronomy & Astrophysics, Volume 645, id.A96, 26 pp.*, 2021.

[9] D. W. Ball, *Field guide to spectroscopy*, vol. 8. Spie Press Bellingham, Washington, 2006.

[10] B. G. Crowther, "Computer modeling of integrating spheres," *Optical Society of America*, 1996.

[11] A. V. Prokhorov and L. M. Hanssen, "Numerical modeling of an integrating sphere radiation source," *Proceedings of SPIE - The International Society for Optical Engineering*, 2002.

[12] R. J. K. Angelo V. Arecchi, Tahar Messadi, *Field Guide to Illumination (SPIE Field Guide Series)*. SPIE Field Guide Series FG11, SPIE Publications, spi ed., 2007.

[13] W. L. Wolfe, *Introduction to Radiometry*. SPIE Press Bellingham, Washington, 1998.

[14] D. G. Goebel, "Generalized integrating-sphere theory," *Applied Optics*, 1966.

[15] V. Sandgren, "Characterization of an integrating sphere radiation reference source," *Chalmers Reproservice*, 2011.

[16] H. F. K. Jonn A. Jacquez, "Theory of the integrating sphere," *Journal of the Optical Socierty of America*, 1954.

[17] T. L. Jeffrey, "Integrating sphere functionality: The scatter transmission measurement." PerkinElmer, Inc.

[18] P. Technologies, “Integrating spheres – introduction and theory.”

[19] W. R. McCluney, *Introduction to Radiometry and Photometry*. ARTECH HOUSE, 2014.

[20] B. G. Grant, *Field guide to radiometry*. SPIE Press Bellingham, Washington, 1957.

[21] International Light Technologies, *INS250 Integrating Sphere Instruction Manual*.

[22] Thorlabs, *∅2” Integrating Sphere*.

[23] Thorlabs, *Fiber-Coupled High-Power LED: M375F2*.

[24] Thorlabs, *Fiber-Coupled LED, 660 nm: M660FP1*.

[25] Thorlabs, *Step-Index Multimode Fiber Optic Patch Cables: SMA to SMA*.

[26] I. Light, “Tungsten halogen lamps gas filled lamps.”

[27] Thorlabs, *PDA36A(-EC) Si Switchable Gain Detector: User Guide*.

[28] Thorlabs, *Compat Photodiode Power Head with Silicon Detector: S120C*.

[29] Ocean Optics, *USB4000 Fiber Optic Spectrometer Data Sheet*.